Spring 5-2014

Design and construction of multi-dimensional optical lattices for 87 Rb Bose-Einstein condensates

Edward Russell Moan
erm8sd@virginia.edu

Design and construction of multi-dimensional optical lattices for ^{87}Rb Bose-Einstein condensates

An Honors Thesis

Presented to the Department of Physics & Astronomy

Bates College

in partial fulfillment of the requirements for the

Degree of Bachelor of Science

by

Edward Russell Moan

Lewiston, Maine

March 21, 2014

Contents

List of Figures

Acknowledgements

First and foremost, I want to thank my family; my parents for their support and for the genetics to complete an honors thesis in experimental physics, and Shane for fostering an extremely competitive sibling rivalry. I owe a lot to the fellow seniors in my lab group, Saad Ansari, Chris Guo, Joanna Moody, and Albert Shi. Throughout this year especially, I have enjoyed working and suffering with them, and appreciate the reminders that I am not in over my head—at least not alone. This year would not have been the same without my friends at Brown House, to whom I am grateful for inducting me as an Honorary Resident. Thank you to Wayne Medlen, who always knows when you need a five minute break from the task at hand. And thank you to Linnea Kaye for forcing me to leave lab on occasion, and for reminding me to eat.

Thank you to the professors in the Bates physics department for the time and effort they put into giving us a great education. During my four years at Bates every one of you has both inspired and frustrated me, and I wouldn't have it any other way. Most importantly, I owe a world of thanks to my advisor, Nathan Lundblad. Since my first year at Bates, Nathan has been an outstanding teacher and I am grateful I've been able to spend the past twelve months working with him. I hope I will be as fortunate as a graduate student, wherever I may be...

Abstract

In recent years, ultracold atomic gases have been used as tools to study strongly-correlated systems reminiscent of interesting systems from solid-state physics. At temperatures just above absolute zero, particles with integer quantum spin ("bosons") begin to congregate in the ground state of the trapping potential. As the temperature of the system falls below a critical temperature T_C (in this experiment near 200 nK) it undergoes a phase transition called Bose-Einstein condensation. A Bose-Einstein condensate is often described as a macroscopic quantum body, and with its phase coherence (analogous to an "atom laser") it can be used to simulate solid-state systems in a periodic potential called an optical lattice, which resembles that experienced by electrons in the periodic Coulomb potential of a solid-state crystal lattice. These optical lattices are formed by the interference pattern of multiple laser beams and the associated spatially-dependent Stark shift, resulting in a periodic trapping potential for the BEC. The lattice analogs of simple atomic structures have been widely studied. In this thesis, we study the possibility of loading a BEC into multi-dimensional optical lattices. The crystallography of four-beam three-dimensional optical lattices is investigated, and an apparatus is constructed to produce two- to four-beam lattice geometries. We study the structure of the lattice through the technique of Kapitza-Dirac scattering.

Introduction

"Go back? No good at all! Go sideways? Impossible!
Go forward? Only thing to do! On we go!"

— J. R. R. Tolkien, *The Hobbit*

Bose-Einstein condensates (BEC) are macroscopic quantum bodies, which can be used experimentally to explore unanswered questions from quantum physics. There is a wide scope of the types of questions we can investigate, such as wave-particle duality using atom interferometry, superfluidity, and quantum vortices. BECs have also been widely used to study solid state crystals by creating analogous optical lattices, and this is the subject of this thesis.

Overview

- A theoretical primer about the laser cooling techniques used to create a ^{87}Rb Bose-Einstein condensate. This begins with a derivation of the condensation temperature from statistical mechanics, followed by an explanation of laser cooling and evaporative cooling techniques.
- The necessary background from solid state physics. This will be important in developing the nomenclature and notation relevant in subsequent chapters, especially relating to the reciprocal lattice.
- A detailed analysis of optical lattices, including an introduction to Bloch waves and Kapitza-Dirac scattering. The solution for a four-beam optical lattice with arbitrary geometry is found, and is applied to lattices in the cubic system.
- A discussion of the experimental apparatus constructed for this thesis. In order to create a four-beam diffraction pattern, a laser beam is split and coupled into four

individual fibers which are sent to the experiment. In addition to detailing the specifics of the apparatus itself, this chapter also includes some discussion of the experimental challenges of realizing a four-beam optical lattice.

- An account of the experimental procedure for realizing Kapitza-Dirac scattering in an optical lattice in one-, two-, and three-dimensions. This begins with aligning the lattice beams individually, and then iteratively optimizing the beam alignments, pulse lengths, and detuning for good scattering.

- In concluding remarks, some of the interesting challenges not discussed in the main text are explained, as well as an outlook of future experiments.

- Appendices include MATHEMATICA code illustrating some of the intensity and optical lattice calculations for geometries in the cubic system.

Chapter 1

Realizing Bose-Einstein condensation

In this thesis an ^{87}Rb BEC is loaded into a multi-dimensional optical lattice. While the bulk of the work on this thesis is related to optical lattice crystallography and the experimental realization of a four-beam lattice, it would be an oversight to forgo an introduction to BEC physics using a statistical mechanics approach, and an overview of the cooling techniques we use in lab.

1.1 Thermodynamics of an ideal Bose system

This section introduces background from statistical thermodynamics of Bose-Einstein condensation, mainly following Pathria's text [3]. The BEC phase transition elegantly follows from applying the Bose-Einstein distribution in the low-temperature limit. The phase transition is an issue of combinatorics of indistinguishable particles [4]. There are a limited number of ways of arranging the particles in excited states, making the ground state heavily favored in the low-temperature limit.

In quantum statistics, there are two ways of arranging non-interacting indistinguishable particles in thermal equilibrium, depending on the particle spins. The average occupation of a state with energy ϵ of bosons, i.e. particles with integer-spin, is given by the Bose-Einstein distribution,

$$\bar{n}_{BE} = \frac{1}{e^{\beta(\epsilon-\mu)} - 1} \tag{1.1}$$

where $\beta = 1/k_B T$. The chemical potential, μ, defines the change in energy when a system accepts or loses a particle. Since there are no restrictions on the number of bosons in the same energy state, the chemical potential is always negative, i.e. an energy state is always

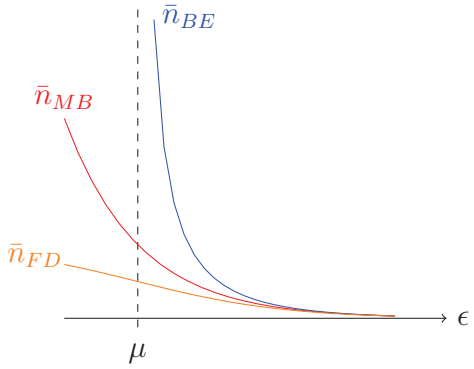

Figure 1.1: Average occupation number of energy states for fermions (orange), bosons (blue), and Maxwell-Boltzmann particles (red). At low temperatures, fermions arrange themselves one-by-one in the lowest available energy state, so the average occupation number converges to 1. There is no maximum occupation number for bosons, so the average occupation number becomes infinitely large. Both distributions converge to the Maxwell-Boltzmann distribution at high temperatures.

willing to receive an additional particle. For fermions, i.e. particles with half-integer spin, the average occupation number is given by the Fermi-Dirac distribution,

$$\bar{n}_{FD} = \frac{1}{e^{\beta(\epsilon-\mu)} + 1} \tag{1.2}$$

In the high-temperature limit, the denominator in both the Fermi-Dirac distribution and the Bose-Einstein distribution become arbitrarily large. The ± 1 becomes negligible, and both reduce to the Maxwell-Boltzmann distribution, as shown in Figure 1.1.

$$\bar{n}_{MB} = \frac{1}{e^{\beta(\epsilon-\mu)}} \tag{1.3}$$

In this limit, the density becomes low enough that classical statistics apply. No two particles will seek a particular energy state, so the quantum statistics become irrelevant. At low temperatures, however, fermions and bosons have radically different behavior. Pauli exclusion requires $\bar{n}_{FD}$ never exceed unity. Each energy state can have an occupation number of 0 or 1. For $\epsilon < \mu$, the mean occupation number tends to 1 as all particles occupy the lowest available states. On the other hand, for a system of bosons, the chemical potential is required to be less than all energy states ($\mu <$ all ϵ). The exclusion principle does not apply, and as μ approaches the lowest energy state ϵ_0, the occupancy of ϵ_0 becomes arbitrarily high, resulting in the formation of a BEC.

Returning to the Bose-Einstein distribution (1.1), we find the total number of particles in a system, which is simply the sum of the average occupation number over all states:

$$N = \sum_s \bar{n}_{BE} = \sum_s \frac{1}{z^{-1}e^{\beta\epsilon} - 1} \tag{1.4}$$

To simplify the following expressions, we introduce the fugacity of the gas, $z = e^{\mu/kT}$. For a large trap volume V, the average occupation spectrum is nearly continuous, which calls for changing the summation in (1.4) to integration. To do this we have to introduce the density of states, which describes the number of available energy states at a given energy:

$$D(\epsilon)\,\mathrm{d}\epsilon = \frac{2\pi V}{h^3}(2m)^{3/2}\sqrt{\epsilon}\,\mathrm{d}\epsilon \tag{1.5}$$

At this step, it is easy to miss a crucial point. Note that the density of states assigns zero weight to the ground state, $\epsilon = 0$. By integrating $\int D(\epsilon)\bar{n}_{BE}\,\mathrm{d}\epsilon$ to find N, we fail to account for the ground state, which obviously becomes a problem in the low-temperature limit. By removing the ground state from the sum before integration, we find

$$N = \frac{2\pi V}{h^3}(2m)^{3/2}\int_0^\infty \frac{\sqrt{\epsilon}}{z^{-1}e^{\beta\epsilon} - 1}\,\mathrm{d}\epsilon + \frac{z}{1-z} \tag{1.6}$$

The last term in (1.6) is the number of particles in the ground state, N_0. The number of particles in excited states is found by subtracting the particles in the ground state:

$$N_{excited} = N - N_0 = \frac{2\pi V(2mk_BT)^{3/2}}{h^3}\int_0^\infty \frac{\sqrt{\epsilon}}{z^{-1}e^{\beta\epsilon} - 1}\,\mathrm{d}\epsilon \tag{1.7}$$

This result can be simplified by substituting $x = \beta\epsilon$, and introducing the Bose-Einstein functions, defined by

$$g_\nu(z) = \frac{1}{\Gamma(\nu)}\int_0^\infty \frac{x^{\nu-1}}{z^{-1}e^x - 1}\,\mathrm{d}x = z + \frac{z^2}{2^\nu} + \frac{z^3}{3^\nu} + ... \tag{1.8}$$

where $\nu \in \mathbb{R}$. Using this result and (1.6), the occupation of the excited states is

$$N_{excited} = \frac{2\pi V(2mk_BT)^{3/2}}{h^3}\int_0^\infty \frac{\sqrt{x}}{z^{-1}e^x - 1}\,\mathrm{d}x = \frac{g_{3/2}(z)}{\lambda^3}V \tag{1.9}$$

where λ is the thermal de Broglie wavelength, given by

$$\lambda = \frac{h}{\sqrt{2\pi m k_B T}} \tag{1.10}$$

For $z \to 1$ and $\nu > 1$, the Bose-Einstein function reduces to the Riemann-zeta function, $\zeta(\nu)$.

$$\lim_{z\to 1} g_\nu(z) = \zeta(\nu) = \sum_{n=1}^{\infty} n^{-\nu} \tag{1.11}$$

For a non-interacting Bose-gas, μ approaches zero from the left in the low-temperature limit. At high temperatures the chemical potential is large and negative. Consequently, the domain of the fugacity is bounded: $0 \leq z \leq 1$. As z approaches unity in the low-temperature limit, the Bose-Einstein function approaches its maximum value equal to the Riemann-zeta function:

$$\lim_{z\to 1} g_{3/2}(z) = \zeta\left(\frac{3}{2}\right) = 2.612 \tag{1.12}$$

Therefore the number of particles in excited states is

$$N_{excited} \leq \zeta\left(\frac{3}{2}\right)\left(\frac{2\pi m k_B T}{h^2}\right)^{3/2} V = 2.612\frac{V}{\lambda^3} \tag{1.13}$$

while the rest of the particles occupy the ground state. For large systems, then, there is a pile-up of particles in the ground state once the excited state occupation reaches its maximum at a given temperature. Clearly this population is non-zero for temperatures above absolute zero, so we always expect both phases to be present when we image the cloud.[1] For fixed values of V and N, we can find the temperature below which particles begin accumulating in the ground state *en masse*, once $N_{excited}$ reaches its upper bound.

$$T < T_c = \frac{h^2}{2\pi m k_B}\left(\frac{N}{\zeta\left(\frac{3}{2}\right)V}\right)^{2/3} \tag{1.14}$$

Here, T_c is the critical temperature. Figure 1.2 shows the complementary fractions of particles in the excited states, and of particles in the ground state.

BEC of an ultracold atomic gas is realized in 3D harmonic traps. Here we do not have a volumetric parameter. Instead, we can relate the number of trapped atoms at criticality to

[1]The two "phases" are the thermal phase and the condensed phase. Because the thermal phase is hotter, we expect a halo to appear around the much denser condensate.

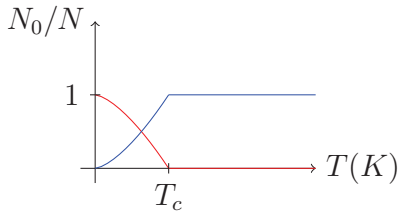

Figure 1.2: Above the condensate temperature T_c, nearly all particles occupy excited states (blue). As the temperature drops below T_c, particles begin to occupy the ground state (red). The population in the excited state reaches naught only at $T = 0$.

the trap frequency, ω_0, and the critical temperature.

$$N \approx \left(\frac{k_B T}{\hbar\omega_0}\right)^3 \tag{1.15}$$

This result can be derived using the thermodynamic potential [3]. From this result we can see that increasing the critical temperature can be achieved by increasing the trap frequency. The proportionality of N and T^3 provides a bit of insight to evaporative cooling techniques discussed later in this chapter. We can selectively remove hotter atoms from the system to significantly lower the temperature of the system, and we can still have large enough populations to reach the BEC transition.

This derivation treats the system as a non-interacting Bose gas. In reality, atoms in the BEC are weakly-interacting. This is corrected by solving a non-linear Schrödinger equation called the Gross-Pitaevskii equation [1]:

$$\left[\frac{\hbar^2}{2m}\nabla^2 + V(r) + g|\psi|^2\right]\psi = E\psi \tag{1.16}$$

The additional term g is the coupling constant. In the Thomas-Fermi approximation, valid for condensates with large populations, the kinetic energy term $\hbar^2\nabla^2/2m$ is neglected [5]. The wavefunction has the form

$$|\psi|^2 = \frac{E - V(r)}{g} \tag{1.17}$$

Therefore the number density takes the form of the harmonic trapping potential. Therefore when image the cloud we expect the BEC profile to be an inverted parabola. Since the cloud is at non-zero temperature, some of the atoms form a thermal cloud that adds a Gaussian component to the density profile.

1.2 Creating an ultracold atomic gas

In order to reach the BEC critical temperature we use a series of optical and magnetic trapping techniques. This section introduces the necessary background from atomic physics, and examines the mechanical forces laser light exerts on an atom. These experimental laser cooling techniques have been well refined, first pioneered by Steven Chu, Claude Cohen-Tannoudji and William Phillips, who won the 1997 Nobel prize for their contributions [6]. All the cooling techniques described in this section exploit one of two forces: either (a) the scattering force due to absorption and spontaneous emission of photons, or (b) the dipole force arising from electric polarizability.

Atoms leaving the effusive oven are slowed first by a 1 meter long Zeeman slower and collected in the magneto-optical trap (MOT). These techniques fall under the umbrella of Doppler cooling, which is limited by the natural line width of the atoms Γ. The magnetic coils are turned off in a brief optical molasses phase, which is limited by the recoil limit. Criticality is reached using evaporative cooling techniques, first in the quadrupole magnetic trap and finally in the optical dipole trap.

Doppler cooling exploits the velocity-dependent frequency shift of light. For a stationary atom in its ground state, there are specific resonant frequencies of incident light that will be absorbed by the atom, moving it to an excited energy state. The photon, approaching from the right, delivers a momentum kick to the stationary atom, $\hbar\mathbf{k}$, so the atom begins to drift to the left. After a short period of time (the lifetime of the excited state of rubidium is 27 ns), the atom reemits the photon as it relaxes to the ground state. This spontaneous emission occurs in a random direction and causes another atom recoil. Continuously repeating this process is called optical pumping [1].

The same effect can be achieved for an atom in motion by exploiting the Doppler shift (see Figure 1.3). An atom moving toward a monochromatic electromagnetic wave will observe red-detuned light, i.e. light at a higher frequency than in a rest frame.

1.2.1 The Zeeman slower

By red-detuning the light source just below resonance, a counterpropagating atom experiences in its frame the resonant frequency, so it absorbs the photon and spontaneously emits as the stationary atom does. The caveat has to do with the speed of the atom. For a given detuning, there is only one good velocity at which the atom can absorb the photon. The photon's momentum kick is small, so in order to effectively cool an atom, it must be opti-

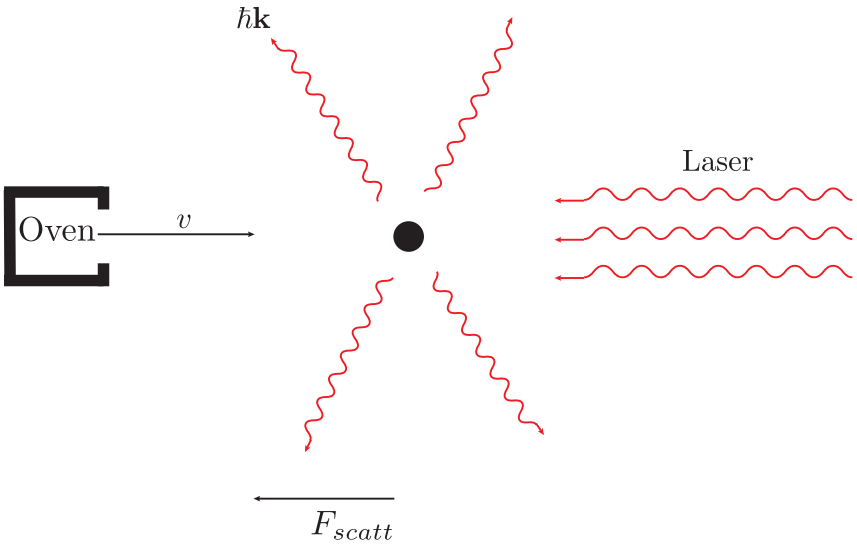

Figure 1.3: Photons absorbed by the atom deliver a momentum kick $\hbar\mathbf{k}$ to the atom antiparallel to its motion. When the atom relaxes a photon is emitted in a random direction. For a large number of optical pumping cycles the momentum kicks of the emitted photons average to zero. A net slowing effect is a result of the initial momentum kick by F_{scatt}. This figure is adapted from Foot [1].

cally pumped a number of times. In order to keep the red-shifted light on resonance with the atom, the line width of the atom can be manipulated with a magnetic field via the Zeeman effect. Assuming the direction of motion along $\hat{\mathbf{z}}$, this frequency shift must obey

$$\omega_0 + \frac{\mu B(z)}{\hbar} = \omega + kv \tag{1.18}$$

On the left-hand side, the resonant frequency ω_0 is increased by a Zeeman shifted term, which depends on the atomic magnetic moment, μ. On the right-hand side the incident photon frequency is increased by the Doppler shift by kv [1]. For a quantum mechanical development of the Zeeman effect see Griffiths [7].

The Zeeman slower was developed by William Phillips and Harold Metcalf [6, 8]. Atoms leaving the effusive oven travel through a tapered solenoid, which produces an inhomogeneous magnetic field. The magnetic field inside the solenoid acts to Zeeman shift the atomic energy levels to match the laser frequency. Upon reaching the end of the slower an atom's temperature drops from 370 K to roughly 1 K. The goal is not to reduce the speed of the atoms to the lower limit of the slower, only to reduce the speed enough that atoms leaving the solenoid are caught in the magneto-optical trap.

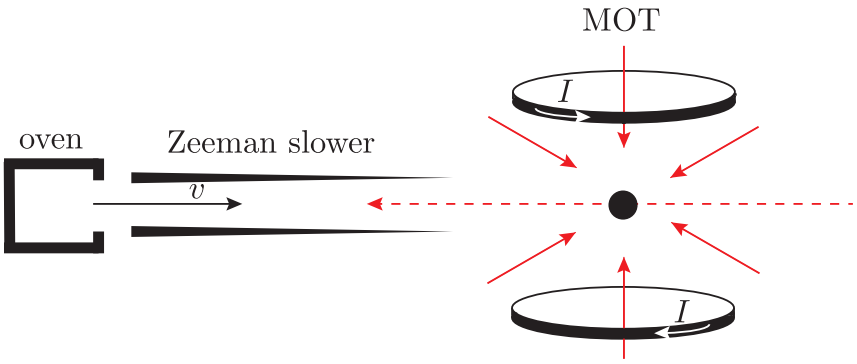

Figure 1.4: Atoms leaving the effusive oven enter the Zeeman slower. Over the course of 1 meter the atoms are optically pumped, and experience a net slowing force from each scattering event. Atoms are kept on-resonance in the Zeeman slower by manipulating the transition frequency using a tapered solenoid. The atom beam is sufficiently slowed such that atoms become trapped in the MOT.

In actuality, this problem becomes more complicated by hyperfine atomic structure. There are two ground hyperfine levels of rubidium, for $F = 1$ and $F = 2$. If the spontaneous emission leaves the atom in the $F = 1$ hyperfine level, the atom will not absorb any incident photons, and remains in this "dark state" in which optical pumping is shut down. To excite atoms out of $F = 1$ an additional laser, the repump laser, is added to excite atoms from the $F = 1$ ground state so they can decay into the $F = 2$ ground state, such that optical pumping can continue.

1.2.2 The magneto-optical trap and optical molasses

Slowed atoms leaving the Zeeman slower are collected in the magneto-optical trap (MOT). The optical configuration requires six lasers, configured in counterpropagating pairs along $\hat{\mathbf{x}}$, $\hat{\mathbf{y}}$, $\hat{\mathbf{z}}$, and a quadrupole magnetic field. The magnetic field is realized by a set of coils in an anti-Helmholtz configuration, which creates a uniform field gradient near the trap center. The three sub-levels of the $J = 1$ state, $M_J = 0, \pm 1$, are Zeeman shifted to vary linearly with position. The MOT, like the Zeeman slower, removes energy from the atoms via the Doppler shift. For an atom displaced from the trap center along $+\hat{\mathbf{z}}$, the $M_J = -1$ moves closer to resonance for a red-detuned laser. The circularly polarized light is absorbed and the atom experiences a force towards the trap center. The same argument is true along all directions.

The MOT is commonly misunderstood as the simple combination of confinement provided

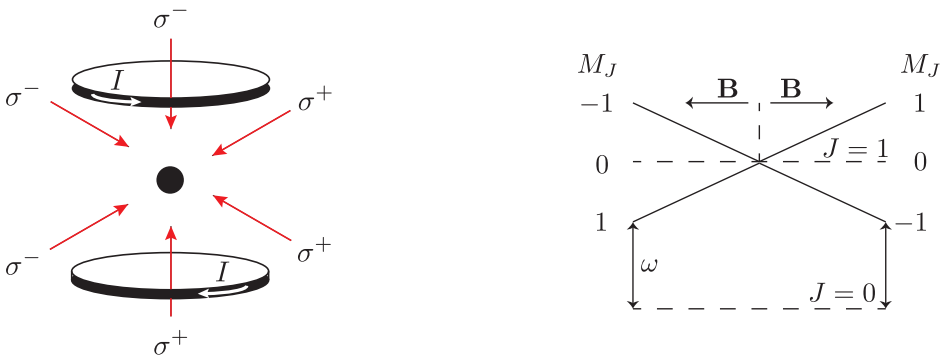

Figure 1.5: Left: The six-beam orientation for the MOT require opposing beams to have oppositely-handed circular polarization. The current in the magnetic coils must be anti-parallel to achieve the anti-Helmholtz configuration. Right: The magnetic coils provide a spatially-dependent Zeeman shift. Atoms further from the trap center experience a higher shift, and become on resonant for slightly red-detuned MOT beams. As a result, they experience a scattering force pushing them towards the center of the trap, where the magnetic field $B = 0$.

by the magnetic field imposed in a region where the six lasers provide cooling. Neither of these components, on its own, can trap the atoms. In actuality, the spatially dependent Zeeman shift punishes atoms for moving away from the trap center by moving them on resonance with a laser. As a result, there is a scattering force pushing the atoms towards the trap center. A typical MOT at Bates has 3×10^9 atoms at roughly 200 μK.

After the MOT reaches a steady state the magnetic coils are turned off for a brief optical molasses phase. One pair of counterpropagating beams with oppositely-handed circular polarizations provide a large velocity-dependent damping force to atoms with sufficiently low velocities to begin with. This is not a trap, however, so the molasses phase is necessarily brief. It acts to cool atoms in the MOT below the Doppler limit at constant density [9]. At the end of the molasses the repump light is turned off, which "depumps" atoms into the $F = 1$ state.

Doppler-cooling techniques of two-level atoms are limited by a competitive heating mechanism, which can be thought of as a random walk in momentum space. The recoil limit is the lowest temperature we can expect to achieve in the molasses phase. Intuition should tell us that there must be a lower limit to Doppler cooling. Each absorption and spontaneous emission process delivers a momentum kick of magnitude $\hbar k$, so the lower limit to the velocity ought to be on the order of the recoil velocity. Any temperature corresponding to a smaller speed would be a peculiar result, given the photon scattering has random directionality. In the lab, temperatures after the MOT phase are actually much hotter than

the Doppler temperature. The limit is surpassed by sub-Doppler cooling techniques in the optical molasses.

1.3 The optical dipole force

As a prelude to a summary of the dipole trap in which the BEC phase transition occurs, this section introduces the Lorentz oscillator model of light-atom interactions. Using this approach we can derive the dipole potential and the scattering rate for an atom in an classically oscillating electric field,

$$\mathbf{E} = E_0 e^{i\omega t} \tag{1.19}$$

where E_0 is the complex amplitude, and ω is the light wave's angular frequency. An atom placed in the electric field will have an induced dipole moment $\mathbf{p}$, which is related to the electric field by the complex polarizability, $\alpha(\omega)$:

$$\mathbf{p} = \alpha(\omega)\mathbf{E} \tag{1.20}$$

The dipole force is conservative, so it can be found by determining the interaction potential. For large oscillation frequencies (a light wave has a period on the order of 10^{-15} s) the resulting interaction potential is given by a time average.

$$U_{dip} = \frac{1}{2}\langle \mathbf{p} \cdot \mathbf{E} \rangle = \frac{1}{2\epsilon_0 c}\mathrm{Re}(\alpha) I \tag{1.21}$$

with the laser field intensity $I = 1/2\epsilon_0 c\, E_0^2$.

Now we can find the scattering rate from the power absorbed by the oscillator. This results from the out-of-phase component of the dipole oscillation, which is described by the imaginary component of the atomic polarizability.

$$P_{abs} = \langle \dot{\mathbf{p}} \cdot \mathbf{E} \rangle = \frac{\omega}{\epsilon_0 c}\mathrm{Im}(\alpha) I \tag{1.22}$$

If instead of a wave the electric field is considered to be a photon beam $\hbar\omega$, the oscillation can be interpreted as absorption and spontaneous emission. Therefore the scattering rate is given by

$$\Gamma_{sc} = -\frac{P_{abs}}{\hbar\omega} = -\frac{1}{\hbar\epsilon_0 c}\mathrm{Im}(\alpha) I \tag{1.23}$$

Now that we have explicit expressions for the dipole potential (1.21) and the scattering

rate (1.23), we can find the frequency-dependent complex polarizability using the Lorentz model of a classical harmonic oscillator [8], in which an electron is bound to the nucleus and orbits with resonant frequency ω_0, which corresponds to the transition frequency. A damping force arrises from dipole radiation. The resulting polarizability is

$$\alpha(\omega) = 6\pi\epsilon_0 c^3 \frac{\Gamma/\omega_0^2}{\omega_0^2 - \omega^2 - i(\omega^3/\omega_0^2)\Gamma} \tag{1.24}$$

where Γ is the on-resonance damping rate given by

$$\Gamma = \frac{e^2\omega_0^2}{6\pi\epsilon_0 m_e c^3} \tag{1.25}$$

For far-off-resonance detuning ($\omega - \omega_0 = \Delta \gg 0$) and sufficiently small intensities (1.24) is valid. But this classical approach ignores the possibility of saturation, which can occur at large intensities and small detuning. The excited state population becomes large, and (1.25) is invalid.

A semiclassical approach is necessary to find the damping, in which the atom is treated as a two-level quantum system interacting with a classical field. The damping rate Γ is determined by the dipole matrix element between the ground state $|g\rangle$ and the excited state $|e\rangle$ of the two-level system,

$$\Gamma = \frac{\omega_0^3}{3\pi\epsilon_0\hbar c^3} \left|\langle e|\boldsymbol{\mu}|g\rangle\right|^2 \tag{1.26}$$

where $\boldsymbol{\mu} = -e\mathbf{r}$ is the quantum mechanical dipole operator. When the detuning is sufficiently small, we can use the rotating wave approximation [1], and can set $\omega/\omega_0 \approx 1$. Therefore the dipole potential and scattering rate can be simplified:

$$U_{dip}(\mathbf{r}) = \frac{3\pi c^2}{2\omega_0^3}\frac{\Gamma}{\Delta} I(\mathbf{r}) \tag{1.27}$$

$$\Gamma_{sc}(\mathbf{r}) = \frac{3\pi c^2}{2\hbar\omega_0^3}\left(\frac{\Gamma}{\Delta}\right)^2 I(\mathbf{r}) \tag{1.28}$$

The dipole potential in (1.27) is negative for red-detuning, meaning $\omega < \omega_0$. The dipole force $\mathbf{F}_{dip} = -\nabla U_{dip}(\mathbf{r})$ is a repulsive force, so atoms will be pushed towards the intensity maxima.

The scattering rate is often expressed in terms of the detuning and the depth of the

dipole potential,

$$\hbar\Gamma_{sc} = \frac{\Gamma}{\Delta} U_{dip} \tag{1.29}$$

The trap depth should ideally be maximized to shut down inelastic scattering and trap the atoms in a conservative potential. Detuning should be maximized—power limitations permitting—since the scattering rate falls off as $1/\Delta^2$, while the potential trap depth falls off only as $1/\Delta$.

1.3.1 Evaporative cooling

In the final stages of realizing BEC, a magnetic trap is used to confine the laser cooled atoms, which are then transferred to an optical dipole trap. In these traps, lower temperatures can be reached with evaporative cooling. With sufficient initial atom count and density, criticality is reached by allowing atoms with more kinetic energy to escape the trap.

After the optical molasses phase, the magnetic trap is turned on and ramped to around 200 G/cm, which requires a current at 32 A. This is much higher than the MOT requires, so a different set of water-cooled coils are used for the magnetic trap. The field is snapped on at 70 G/cm in the vertical direction, which matches the size of the atom cloud. The field is ramped to 200 G/cm over 200 ms. Forgoing the ramp to a high gradient would result in significant heating because the trapping region is too small. Ramping the trap to a tight confinement does result in adiabatic heating, but the trap shape greatly increases the density.

In a magnetic field, the potential of a dipole is

$$U = -\boldsymbol{\mu} \cdot \mathbf{B} \tag{1.30}$$

From this potential the magnetic force can be found:

$$\mathbf{F} = \mu_l \nabla \mathbf{B} \tag{1.31}$$

where μ_l is the projection of the magnetic moment onto the direction of the field. At this stage, the atomic spin becomes relevant. Only one of the three spin states, $M_F = 1$, experiences confinement. In principle, this eliminates 1/3 of the atoms trapped in the MOT in order to achieve colder temperatures, but experimental figures show fraction closer to 1/2 in the trapped state.

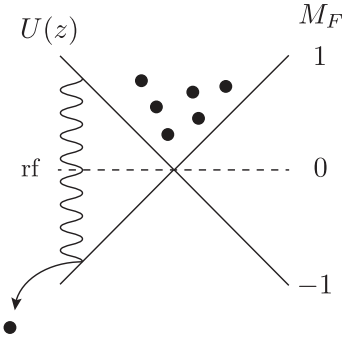

Figure 1.6: The rf sweep forces hotter atoms located higher in the trap to spin-flip and escape the trap. Upon rethermalization, the cloud has higher density and lower temperature.

The quadrupole magnetic coils produce a linear potential near the trap center with

$$\frac{\mathrm{d}\mathbf{B}}{\mathrm{d}x}\,\hat{\mathbf{x}} = \frac{\mathrm{d}\mathbf{B}}{\mathrm{d}y}\,\hat{\mathbf{y}} = -\frac{1}{2}\frac{\mathrm{d}\mathbf{B}}{\mathrm{d}z}\,\hat{\mathbf{z}} \tag{1.32}$$

The factor of 1/2 in the $\hat{\mathbf{z}}$ component originates from Maxwell's equations, requiring that $\nabla\mathbf{B} = 0$. In the quadrupole magnetic trap, sub-Doppler cooling is realized by evaporatively cooling using an radio-frequency (rf) sweep, which induces a transition between trapped and untrapped ($M_F = \pm 1$) Zeeman levels. The atoms in the trap have a Boltzmann distribution, and hotter atoms in the trapped cloud spend more time at higher energy. Sweeping the rf "knife" from the top down essentially lowers the trap depth, allowing these hotter atoms to escape. While the cloud now has fewer atoms, upon rethermalization through elastic collisions it has lower temperature and higher phase-space density [5].

The shortcoming of the quadrupole trap has to do with the field-zero at the center. While an atom is in a region of non-zero magnetic field, its spin is well-defined, unlike at the trap center where $B = 0$. For a slow atom crossing the trap center, the magnetic moment is unable to adiabatically follow the sudden change in the magnetic field. As a result, the atom undergoes Majorana spin-flip, and is no longer trapped. This phenomenon results in significant losses, especially for colder clouds in which atoms spend more time at lower potential near the zero-crossing [10].

There are several methods of eliminating Majorana losses in the quadrupole trap. In this experiment we add an optical dipole trap, which pulls the atoms away from the zero-crossing so their spin remains well-defined. To transfer atoms to the dipole trap, the quadrupole field gradient is ramped adibatically down to 30 G/cm over 2 s. This is slightly less than the gravitational field, allowing the atoms to fall into the dipole trap. The 6.0 W ($\lambda = 1060$ nm)

tightly focused beam is aligned roughly 100 μm below the magnetic zero-crossing.

The combination of the magnetic and dipole trap has an effective potential depicted in Figure 1.7. For $x = y = 0$, this is given by

$$U(z) = \mu z \frac{\mathrm{d}\mathbf{B}}{\mathrm{d}z} - U_0 \exp\left[-2\frac{(z-z_0)^2}{w_0^2}\right] + mgz + E_0 \tag{1.33}$$

where U_0, w_0, and z_0 are the trap depth, waist, and offset from the magnetic trap center (at $z = 0$) of the dipole beam [10]. The term mgz is the gravitational contribution, and E_0 is the displacement between the trap minimum and the magnetic trap zero.

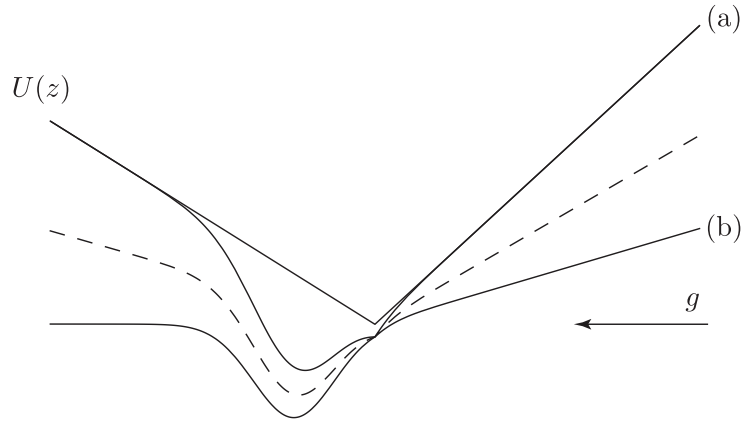

Figure 1.7: In the magnetic trap (a), evaporative cooling is limited by Majorana losses because of the cusp at the zero-crossing. Transferring the atoms from the magnetic trap into the dipole trap is done by ramping the field gradient to 30 G/cm (b) over 2 seconds, such that it just supports against gravity. After transferring into the dipole trap, further evaporative cooling is carried out.

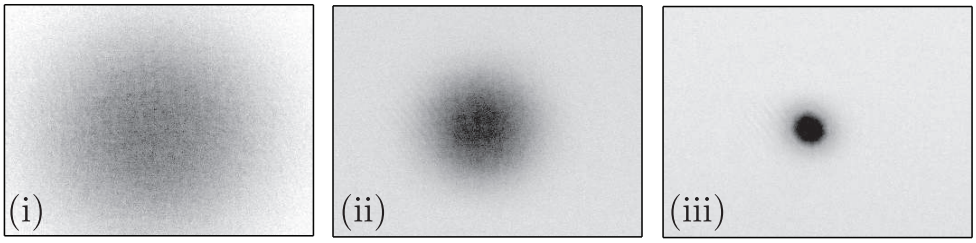

Figure 1.8: Absorption images after 15 ms time-of-flight. (i) and (ii) are thermal clouds, and (iii) is a BEC. Note the bimodal distribution in (iii), i.e. the presence of both the thermal halo surrounding the condensed phase. The temperature of the clouds, from left to right, are 1800 nK, 400 nK, and < 100 nK.

At this stage, the temperature of the cloud of roughly ten billion atoms is on the order of 10 μK. The final step towards BEC is forced evaporative cooling in the dipole trap. The principle is the same as the evaporative cooling in the quadrupole trap. By lowering the depth of the dipole trap, and simultaneously reducing the magnetic field gradient such that it no longer supports against gravity, atoms with higher energy escape. BEC is reached when the phase-space density is on the order of 1.

$$1 \propto N \left(\frac{\hbar \bar{\omega}}{k_B T} \right)^3 \tag{1.34}$$

For typical trap frequencies on the order of 50 Hz the condensate temperature $T_c \approx 200$ nK. Our apparatus reliably produces BEC of ^{87}Rb with temperatures below 100 nK. The typical atom count is on the order of 2×10^5 atoms, with densities on the order of 10^{13} cm^{-1}. To recap the cooling process:

1. Atoms leaving the effusive oven are slowed by a radiation scattering force in the Zeeman slower. The atoms are Doppler shifted in order to keep the laser on-resonance with the laser.

2. Atoms leaving the slower are collected in the MOT, where they are cooled by a radiation scattering force towards the trap center. The magnetic field creates a spatially-dependent Zeeman shift, such that atoms moving away from the trap center are on-resonance with the lasers.

3. The MOT coils are turned off and the atoms undergo sub-Doppler cooling in a brief optical molasses phase, followed by optical depumping into $F = 1$.

4. The quadrupole magnetic field is snapped on and adibatically ramped to a tight confinement. Evaporative cooling in the magnetic trap is realized by an rf sweep that expels higher-energy atoms. This process is limited by Majorana losses at the zero-crossing.

5. Atoms are transferred into the dipole trap by lowering the magnetic field gradient. Forced evaporation is realized by reducing the intensity of the dipole beam, which lowers the trap depth. This process achieves sufficiently high density and low temperature for Bose-Einstein condensation to occur.

1.3.2 Imaging technique

A key component of the experimental setup is imaging system. In order to image the cloud, an additional probe laser must be used, shown in Figure 1.9. The cloud is released from the dipole trap and after a brief period of ballistic expansion of 15 ms the probe laser is pulsed. This laser is on-resonance with the atoms and is absorbed, effectively destroying the BEC. An objective lens is positioned a focal length behind the cloud, collimating the unabsorbed light passing around the cloud. This light is focused into a CCD camera. After the cloud has dispersed the probe laser is pulsed again. The background is subtracted from the two images, which are then divided to produce an image of the cloud.

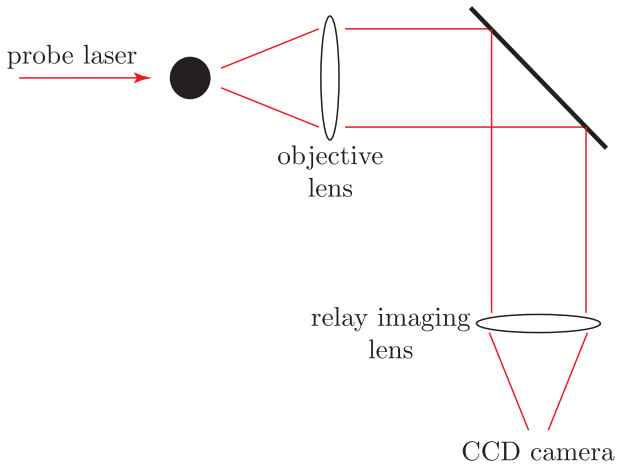

Figure 1.9: Optical diagram of the imaging system. An on-resonant probe beam is pulsed and the time-of-flight image is collected in a CCD camera. A second image is required to subtract the background and produce a final image of the cloud.

The detection of BEC has to do with the characteristic profile of the cloud. A cloud that has not reached sufficient temperature and density for BEC is still in the thermal regime, and can therefore be well-fit to a Gaussian distribution. The parameters of this fit provide information about temperature and density of the thermal cloud. For samples that have reached the BEC phase transition, Boltzmann statistics no longer apply and the Gaussian fit fails.

The absorption profile of a BEC has a parabolic distribution near the cloud center, as predicted by the Thomas-Fermi approximation, in addition to a thermal halo around the BEC. The best-fit, then, is the sum of the Gaussian distribution and an inverted parabola. We image the time-of-flight, which is a momentum distribution. The information we can access for an absorption image is only the density distribution after ballistic expansion for a known time-of-flight. By finding the width of the Gaussian fit, we can find the thermal speed distribution of the atoms, i.e. the momentum distribution. We can find the temperature of the cloud using statistical mechanics. The importance of this distinction will be clear for absorption images of atoms in an optical lattice, since the momentum distribution is the reciprocal lattice.

Chapter 2

Periodic crystal structures

To simulate real crystal structures in optical lattices, we first need to know something about the crystal structure itself. The following chapter introduces some of the important nomenclature from solid state physics, and details the fundamental concepts that will be relevant to optical lattice physics. The most important concept from solid state physics is the reciprocal lattice, which is the Fourier transform of the lattice. More often than not, we have access to information about the reciprocal lattice only, which we can use to extract the nature of the direct lattice. This chapter roughly follows Kittel's solid state text [11].

2.1 The crystal lattice and the basis

An ideal crystal is a periodic infinite array of identical groups of atoms. One individual group is called the basis. Each basis is associated with a mathematical point, and the set of all these points makes up lattice. In three dimensions, this set is defined by three translation vectors, $\mathbf{a}_1$, $\mathbf{a}_2$, $\mathbf{a}_3$, such that any integral linear combination defines a translation from one lattice site to another. I.e. at an arbitrary point $\mathbf{r}$, any other point $\mathbf{r}'$ must be

$$\mathbf{r} = \mathbf{r}' + u_1\mathbf{a}_1 + u_2\mathbf{a}_2 + u_3\mathbf{a}_3 \tag{2.1}$$

where u_1, u_2, u_3 are integers. The lattice is the set of points $\mathbf{r}'$ defined in (2.1) for all u_1, u_2, u_3. The set of all $\mathbf{r}'$ is contained in $\{\mathbf{T}\}$, the direct lattice. The translation vectors define the crystal axes. When the lattice looks identical at each site—when all points have the same arrangement of nearest neighbors—it is said to be Bravais.

Once the translation vectors are chosen, we can consider all the atoms in the basis. A

multi-atom basis can be mathematically expressed using the translation vectors:

$$\mathbf{r}_j = x_j\mathbf{a}_1 + y_j\mathbf{a}_2 + z_j\mathbf{a}_3 \tag{2.2}$$

Here, the origin is an arbitrary lattice site, meaning $0 \leq x_j, y_j, z_j \leq 1$. This is a mathematical construction, and it is not unique. Often there are multiple convenient choices for the same structure, but it is usually simpler to minimize the number of atoms in a basis, as long as the periodicity condition still holds. In other cases, like within the cubic system, there are more intuitive choices for the basis vectors.

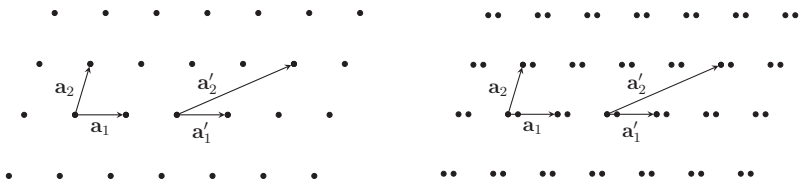

Figure 2.1: A small area of a two-dimensional lattice may be the same for two different structures. For both (a) and (b) the choice of the basis vectors $\mathbf{a}_i$ are not unique. While (b) has a different structure than (a), the basis vectors chosen are the same, only in this case we must consider a two-atom basis as well.

2.2 Three-dimensional lattices

There are fourteen different lattice types in three dimensions, which fall into one of the seven systems in Table 2.1. Here, the focus will be on the cubic system, of which there are three Bravais lattices, viz. simple cubic (sc), face-centered cubic (fcc), and body-centered cubic (bcc).

The conventional bcc and fcc cells are not primitive for convenience; they contain two and four lattice points respectively. The origin is chosen to be the corner of a cubic cell. The second basis lattice point in a bcc in the middle of the cube at $\frac{1}{2}\frac{1}{2}\frac{1}{2}$. In the fcc lattice the additional basis points are halfway up the three adjacent diagonals of the cube at $\frac{1}{2}\frac{1}{2}0$, $\frac{1}{2}0\frac{1}{2}$, and $\frac{1}{2}\frac{1}{2}0$.

The diamond cubic crystal structure is adopted by certain elements in group 14 in their solid forms. The diamond lattice can be considered a face-centered cubic structure with a two-atom basis. Each atom in the face-centered cubic structure is associated with an identical atom up the diagonal at $\frac{1}{4}\frac{1}{4}\frac{1}{4}$. Since there are four points in the conventional unit

System	Number of lattices	Restrictions
Triclinic	1	$a_1 \neq a_2 \neq a_3$ $\alpha \neq \beta \neq \gamma$
Monoclinic	2	$a_1 \neq a_2 \neq a_3$ $\alpha = \gamma = 90° \neq \beta$
Orthorhombic	4	$a_1 \neq a_2 \neq a_3$ $\alpha = \beta = \gamma = 90°$
Tetragonal	2	$a_1 = a_2 \neq a_3$ $\alpha = \beta = \gamma = 90°$
Cubic	3	$a_1 = a_2 = a_3$ $\alpha = \beta = \gamma = 90°$
Trigonal	1	$a_1 \neq a_2 \neq a_3$ $\alpha = \beta = \gamma < 120°, \neq 90°$
Hexagonal	1	$a_1 = a_2 \neq a_3$ $\alpha = \beta = 90°$ $\gamma = 120°$

Table 2.1: There are seven types of three-dimensional systems. a_1, a_2, a_3 are the lengths of the unit vectors. α, β, γ are the angles between the basis vectors, as shown for the triclinic lattice in Figure 2.2.

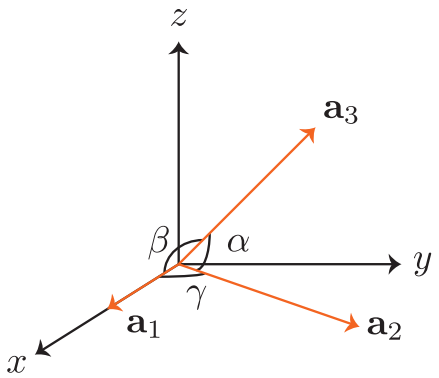

Figure 2.2: The lattice vectors for the triclinic lattice. (See Table 2.1.) The coordinate system is chosen such that $\mathbf{a}_1$ points along $\hat{\mathbf{x}}$, and $\mathbf{a}_2$ is in the xy plane.

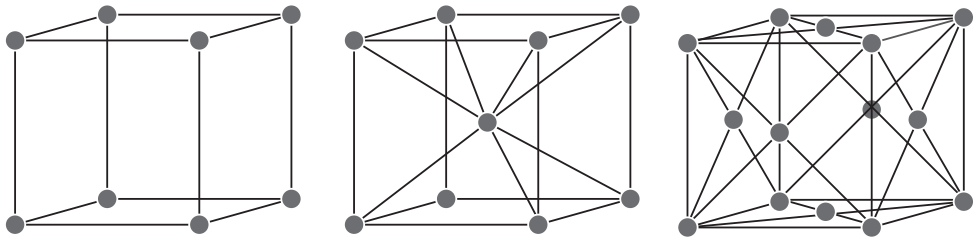

Figure 2.3: The three Bravais lattices in the cubic system. From left to right: sc, bcc, fcc.

cell of the fcc, the conventional diamond cell must have eight. There is no possible way to express the diamond lattice as Bravais.

2.3 Reciprocal space

So far we have examined the lattice in real space. In solid state physics it is often advantageous to examine the reciprocal lattice, which lives in momentum space, or reciprocal space. We can use diffraction techniques to learn about the reciprocal lattice of a crystal, which is rich with information about the geometry of the direct lattice. For wavelengths on the order of the inter-planar distance in the crystal structure, the resulting diffraction pattern obeys Bragg's law, which states that the constructive interference of light reflecting from two adjacent planes is given by

$$2d \sin\theta = n\lambda \tag{2.3}$$

This is a useful tool for analyzing the periodicity of the lattice.

From (2.1) it is clear that the lattice has periodicity. Explicitly, the electron number density $n(\mathbf{r})$ is invariant under translations along $\mathbf{a}_1$, $\mathbf{a}_2$, $\mathbf{a}_3$ for integer combinations of u_1, u_2, u_3. This periodicity is of the form $n(\mathbf{r}+\mathbf{r}') = n(\mathbf{r})$. The periodicity of the lattice is ideal for Fourier analysis techniques. For a one-dimensional lattice with lattice constant a, we can write $n(x)$ as a Fourier series of plane waves:

$$n(x) = n_0 + \sum_{p>0} C_p \cos(2\pi px/a) + S_p \sin(2\pi px/a) \tag{2.4}$$

where p is a positive integer, and C_p and S_p are the Fourier coefficients. In order to ensure

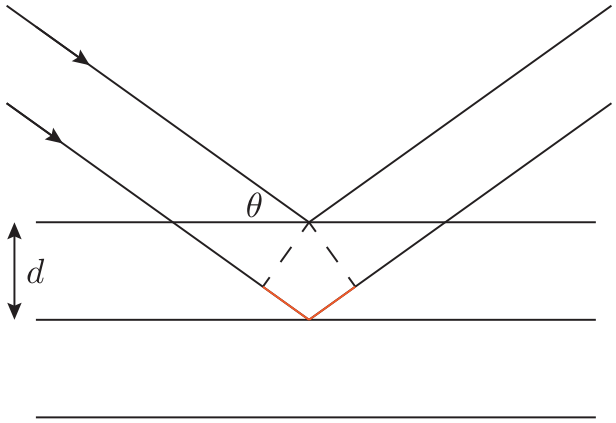

Figure 2.4: Bragg diffraction occurs for plane waves hitting two adjacent planes in the lattice. The orange segment of the lower beam path is the extra distance that light travels, which is $2d\sin\theta$.

$n(x)$ has the correct periodicity, we include the factor of $2\pi/a$ in the Fourier series.

$$\begin{aligned} n(x+a) &= n_0 + \sum_{p>0} C_p \cos(2\pi px/a + 2\pi p) + S_p \sin(2\pi px/a + 2\pi p) \\ &= n_0 + \sum_{p>0} C_p \cos(2\pi px/a) + S_p \sin(2\pi px/a) \end{aligned} \tag{2.5}$$

The allowed points in the Fourier series of $n(x)$ compose the reciprocal lattice. Note that the distance between points in reciprocal space is the inverse of the separation in the direct lattice. The units of the direct lattice are [length], and the units of the reciprocal lattice are [1/length]. This argument extends to higher dimensions as well. Written in a more compact exponential form,

$$n(\mathbf{r}) = \sum_{\mathbf{G}} n_{\mathbf{G}}\, e^{i\mathbf{G}\cdot\mathbf{r}} \tag{2.6}$$

Here, $\mathbf{G}$ is the set of translational vectors in k-space that correspond to the allowed translations in the direct lattice. To maintain the periodicity in both the direct and reciprocal lattices,

$$\mathbf{b}_i \cdot \mathbf{a}_j = 2\pi\delta_{ij} \tag{2.7}$$

where $\mathbf{b}_i$ and $\mathbf{a}_i$ are the reciprocal and direct lattice vectors, respectively. The basis vectors of the reciprocal lattice are constructed from the direct lattice vectors:

$$\mathbf{b}_1 = \frac{2\pi}{a}\frac{\mathbf{a}_2 \times \mathbf{a}_3}{\mathbf{a}_1 \cdot \mathbf{a}_2 \times \mathbf{a}_3}; \mathbf{b}_2 = \frac{2\pi}{a}\frac{\mathbf{a}_3 \times \mathbf{a}_1}{\mathbf{a}_1 \cdot \mathbf{a}_2 \times \mathbf{a}_3}; \mathbf{b}_3 = \frac{2\pi}{a}\frac{\mathbf{a}_1 \times \mathbf{a}_2}{\mathbf{a}_1 \cdot \mathbf{a}_2 \times \mathbf{a}_3}; \tag{2.8}$$

The denominator is simply the volume of the primitive cell. It can also be shown that the Fourier transform of the reciprocal lattice is the direct lattice. The reciprocal lattice is mathematically described in the same way as the direct lattice:

$$\mathbf{G} = v_1\mathbf{b}_1 + v_2\mathbf{b}_2 + v_3\mathbf{b}_3 \tag{2.9}$$

where, again, v_i must be integers. Any crystal lattice has two lattices associated with it, and can be described by either the direct or reciprocal lattice. All points in the reciprocal lattice are described in Fourier space, which is conveniently also how we describe wavevectors. Any diffraction technique provides information in momentum space, where the allowed translations are permitted momentum changes. As it turns out, a diffraction pattern of a crystal is a map of the crystal's reciprocal lattice.

Let us derive the reciprocal lattice of the fcc lattice. Recall the primitive translation vectors for the fcc lattice:

$$\mathbf{a}_1 = \frac{a}{2}(\,\hat{\mathbf{y}} + \hat{\mathbf{x}});\ \mathbf{a}_2 = \frac{a}{2}(\,\hat{\mathbf{x}} + \hat{\mathbf{z}});\ \mathbf{a}_3 = \frac{a}{2}(\,\hat{\mathbf{x}} + \hat{\mathbf{y}}) \tag{2.10}$$

Using (2.8) we can find the reciprocal lattice vectors. The volume of the primitive cell is $V = |\mathbf{a}_1 \cdot \mathbf{a}_2 \times \mathbf{a}_3| = \frac{a^3}{4}$.

$$\mathbf{b}_1 = \frac{2\pi}{a}(-\,\hat{\mathbf{x}} + \hat{\mathbf{y}} + \hat{\mathbf{z}});\ \mathbf{b}_2 = \frac{2\pi}{a}(\,\hat{\mathbf{x}} - \hat{\mathbf{y}} + \hat{\mathbf{z}});\ \mathbf{b}_3 = \frac{2\pi}{a}(\,\hat{\mathbf{x}} + \hat{\mathbf{y}} - \hat{\mathbf{z}}) \tag{2.11}$$

Referring back to Table 2.1, these are the basis vectors for the body-centered cubic direct lattice. This is a critical result, and as a consequence of the inverse Fourier transform, the reciprocal of the bcc lattice has an fcc geometry.

Chapter 3

Optical lattice crystallography

Intersecting laser beams interfere with each other and can form stable periodic potentials that trap neutral atoms. The trapping mechanism is the AC Stark shift, a perturbation introduced by an oscillating electric field [1]. The interference pattern forms an optical lattice, in which atoms act as the analog of electrons in real crystal structures.

A Gaussian laser beam, such as the optical dipole trap discussed in Chapter 2, has an intensity profile

$$I(r,z) = \frac{2P}{\pi w^2(z)} e^{\frac{-2r^2}{w^2(z)}} \tag{3.1}$$

where $w(z) = w_0\sqrt{1+(z/z_R)^2}$ is the $1/e^2$ radius, $z_R = \pi w^2/\lambda$ is the Rayleigh length, and P is the laser power [2]. The maximum intensity $I_0 = 2P/\pi w_0^2$. By superimposing two or more Gaussian beams, we can realize a periodic optical potential. The simplest case is a beam retroreflected, which forms a standing wave. This forms a one-dimensional lattice with a half-wavelength period. The potential of the optical trap for a beam propagating along $\hat{\mathbf{z}}$ is given by

$$V(r,z) = -V_{lat}\, e^{-2r^2/w_0}\, \sin^2(kz) \tag{3.2}$$

V_{lat} is the trap depth, and $k = 2\pi/\lambda$ is the wavevector. Higher dimensional optical traps are realized by interfering multiple beams. For two beams arranged orthogonally along $\hat{\mathbf{x}}$ and $\hat{\mathbf{y}}$, the superimposed waves create a trapping potential

$$V(x,y) = -V_{lat}\left[\cos^2(kx) + \cos^2(ky) + 2\boldsymbol{\epsilon}_1 \cdot \boldsymbol{\epsilon}_2 \cos\phi \cos(kx)\cos(ky)\right] \tag{3.3}$$

where k is the magnitude of the wavevector, $\boldsymbol{\epsilon}_i$ are the polarizations unit vectors, and ϕ is the time phase between the beams. The phases can be stabilized, so $\cos\phi = 1$. The third term

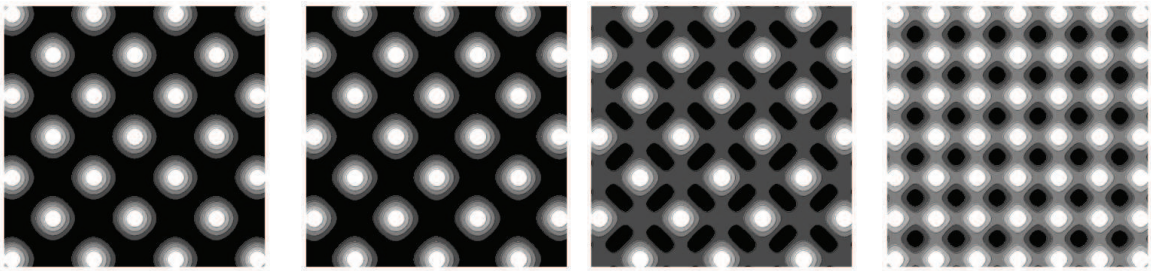

Figure 3.1: 2D lattice potentials formed by two counterpropagating orthogonal beams with various polarization overlap. For red-detuned light, atoms seek the lighter regions of the contour plot. From left to right, the angle between $\boldsymbol{\epsilon}_1$ and $\boldsymbol{\epsilon}_2$ is 0°, 30°, 60°, and 90°. In the last case the polarizations are perfectly orthogonal and the beams are unaffected by each other. For non-zero angles this potential resembles a square lattice with a two atom basis [2].

accounts for the interference between the two beams, which is determined by the overlap of their polarization vectors. If these are not orthogonal the beams interfere with each other, resulting in checkerboard-like lattices illustrated in Figure 3.1. This has been extended to three dimensions by adding a retroreflected beam along $\hat{\mathbf{z}}$ [2].

3.1 Bloch waves & Kapitza-Dirac scattering

This section investigates how turning on the optical lattice affects the atoms. This, of course, occurs once they have reached BEC in the optical dipole trap. One of the important parameters not yet mentioned is the pulse length of the lattice beams. In this experiment the pulse lengths are very short; the width of the pulse in momentum space (i.e. its Fourier width) is larger than the distance between neighboring momentum states [12]. In this regime, the atoms are treated as stationary, and the lattice potential can be expressed in the form

$$V(z,t) = -V_0 f^2(t) \sin^2(kz) \tag{3.4}$$

where V_0 is the trap depth, and $f(t)$ is shape of the lattice pulse. This can be treated with the eikonal approximation for partially expanded waves [13]. Given the initial wavefunction of the system $|\psi_0\rangle$, the wavefunction shortly after the lattice is turned on is

$$|\psi\rangle = e^{\frac{-i}{\hbar}\int V(z,t)\,\mathrm{d}t} = |\psi_0\rangle\; e^{-iV_0\tau/\hbar}\; e^{-iV_0\tau\cos(2kz)/\hbar} \tag{3.5}$$

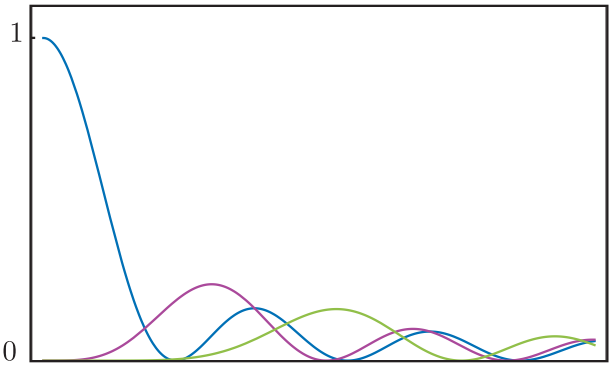

Figure 3.2: Bessel functions of the first type for $N = 0, 2, 4$. These can be fitted to the fractional occupation of the N^{th} eigenstate $|2N\hbar k\rangle$.

where $\tau = \int f^2(t)\ \mathrm{d}t$ is the integral over the pulse length. This result is often expressed in terms of the Bessel functions of the first kind [14, 12], which are of the form

$$e^{i\alpha\cos\beta} = \sum_{n=-\infty}^{\infty} (i)^n J_n(\alpha) e^{in\beta} \tag{3.6}$$

Therefore the wavefunction is written as

$$|\psi\rangle = |\psi_0\rangle\ e^{-iV_0\tau/2\hbar} \sum_{n=-\infty}^{\infty} (i)^n J_n\left(\frac{V_0\tau}{2\hbar}\right) e^{i2nkz} \tag{3.7}$$

The position space representation of momentum $|g, p\rangle = \mathcal{N} e^{ipz/\hbar}$ can be used, where $\mathcal{N}$ is a normalization constant. If the initial momentum is naught, the wavefunction becomes

$$|\psi\rangle = e^{-iV_0\tau/2\hbar} \sum_{n=-\infty}^{\infty} (i)^n J_n\left(\frac{V_0\tau}{2\hbar}\right) |g, 2n\hbar k\rangle \tag{3.8}$$

Therefore the probability of an atom being in the N^{th} energy state (with $p_N = 2N\hbar k$) is

$$P_N = J_N^2(V_0\tau/2\hbar) \tag{3.9}$$

This result is especially interesting in the context of solid state physics. Bloch's theorem restricts the form of the wavefunction of electrons in a crystal lattice, and this result is also true for atoms in an optical lattice [2]. The solution to Schrödinger equation for a periodic potential must have the form

$$\psi_q^{(n)}(z) = e^{iqx/\hbar} \cdot \phi_q^{(n)}(z) \tag{3.10}$$

Here, n is the Bloch band index, $q = \hbar k$ is the quasi-momentum, and $\phi_q^{(n)}$ is a function with the same periodicity as the lattice. This means eigenfunctions must be the product of a plane wave and a periodic function with the same periodicity as the potential. This result comes from the requirement of invariance under translation, i.e. $V(z) = V(z+a)$. By fiat, the periodic term in (3.10) can be expanded as Fourier series over the reciprocal lattice vectors, $\mathbf{G}$. This result can be found by deriving the central equation.[1]

A condensate is a plane wave $\phi_q(t)$ with quasi-momentum q. This can be written as a superposition of Bloch states $|n, q\rangle$ by expanding in the Bloch basis:

$$|\psi_0\rangle = \sum_{n=0}^{\infty} |n, q\rangle\langle n, q|\phi_q\rangle \tag{3.11}$$

Here, $\langle n, q|\phi_q\rangle = c_{n,q}(0)$. If an optical lattice is suddenly turned on for a time τ, each eigenstate evolves with its respective energy, and the condensate wavefunction evolves in time:

$$|\psi\rangle = \sum_{n=0}^{\infty} c_{n,q}(0)\ e^{iE_n(q)t/\hbar}\ |n, q\rangle \tag{3.12}$$

Bloch's theorem applies only through the duration of the pulse. Once the periodic potential is turned off, to find the wavefunction we must map the Bloch states back to a plane wave basis by multiplying by the phase factor

$$d_q(j) = \sum_{n=0}^{\infty} c_{n,q}(0)\ c_{n,q}(j)\ e^{iE_n(q)t/\hbar} \tag{3.13}$$

The wavefunction in a plane wave basis is

$$|\psi_\tau\rangle = \sum_{n=0}^{\infty} d_j(q)|\phi_{q+2j\hbar k}\rangle \tag{3.14}$$

Since the condensate begins at rest, only the even ordered energies are occupied, which is true for Kapitza-Dirac scattering in (3.8). In other words, the population in the $|2j\hbar k\rangle$ eigenstates oscillates with time for Kapitza-Dirac scattering. The momentum change of two photons comes from the requirement of two beams [12]. Note that this is not the case for a condensate with non-zero initial momentum because the wavefunction is not symmetric. In this case, Bragg scattering can occur. For near-resonant light and sufficiently short pulse

[1]For a rigorous derivation of the wave equation of an electron in a periodic potential see Kittel [11].

lengths of two or more lattice beams, we see Kapitza-Dirac scattering when we image the BEC. The time-of-flight imaging is a momentum distribution. Therefore Kapitza-Dirac scattering contains information about the reciprocal lattice.

3.2 Four-beam optical lattices

Periodic interference patterns with four-beam geometries have been well developed for research relating to optical photonics. The methods for finding a specific structure are well-known, and the main results are summarized here. The endgame of the mathematical development is to determine how a four-beam geometry produces a specific time-of-flight image. There are many parameters to consider in addition to the orientation of the beams; viz. the polarizations and intensities of the individual beams.

The analysis of a 3D four-beam geometry becomes overwhelming in any conventional coordinate system. It is convenient to develop a set of orthonormal triads for each normalized propagation vector, $\mathbf{k}_i$. Following Toader [15], let $\mathbf{R}_i = \mathbf{k}_i \times \hat{\mathbf{z}}$, $\mathbf{U}_i = \mathbf{R}_i \times \mathbf{k}_i$, and $\mathbf{U}_i \times \mathbf{R}_i = \mathbf{k}_i$. If for the chosen cartesian reference frame ($\hat{\mathbf{x}}$, $\hat{\mathbf{y}}$, $\hat{\mathbf{z}}$) the beam propagates along $\hat{\mathbf{z}}$, then by convention let $\mathbf{R}_i = \hat{\mathbf{x}}$. The polarization vector, $\boldsymbol{\epsilon}_i$, in this beam coordinate system is a linear combination of $\mathbf{R}_i$ and $\mathbf{U}_i$, parameterized by a rotation angle about $\mathbf{k}_i$, letting $\mathbf{U}_i$ be the azimuthal origin.

Determining the geometry of the intensity pattern of interfering laser light has been extensively explored for creating photonic crystals [16, 17]. The approach to optical lattice geometry is identical, but the existing apparatus turns out to be the limiting factor in realizing some of these lattices. The wave design for producing any of the fourteen Bravais lattice geometries can be found with the following approach, beginning with the trapping potential of four interfering non-coplanar beams. Each of these beams has the same wavelength λ, and the j^{th} beam produces a plane wave of the form

$$\mathbf{E}_j = E_j e^{i\mathbf{k}_j \cdot \mathbf{r}} \boldsymbol{\epsilon}_j \tag{3.15}$$

where E_j is the real amplitude, $\boldsymbol{\epsilon}_j$ is the normalized polarization of the wave, and $\mathbf{k}_j$ is the normalized wavevector,

$$\mathbf{k}_j = \frac{2\pi}{\lambda}(l_j, m_j, n_j) \tag{3.16}$$

where l_j, m_j, n_j are projections of the wavevector to a common coordinate system. The

resulting intensity of the four-beam interference is

$$I = \sum_{j=1}^{4} E_j^2 + 2 \sum_{i<j} E_i E_j \epsilon_{ij} \cos[(\mathbf{k}_i - \mathbf{k}_j) \cdot \mathbf{r}] \tag{3.17}$$

where $\epsilon_{ij} = |\boldsymbol{\epsilon}_i \cdot \boldsymbol{\epsilon}_j|$. We need only examine the interaction of three arbitrarily chosen cross-terms from (3.17), as the other interactions are inherently determined by the chosen interactions. From the interactions between the first beam $\mathbf{E}_1$ and the other three beams, the interference pattern has maxima when

$$\cos[(\mathbf{k}_1 - \mathbf{k}_2) \cdot \mathbf{r}] = \cos(\mathbf{k}_1 - \mathbf{k}_3) \cdot \mathbf{r} = \cos(\mathbf{k}_1 - \mathbf{k}_4) \cdot \mathbf{r} = 1 \tag{3.18}$$

For simplicity, consider the first term in (3.18). Using (3.16) for the wavevector, the argument of the cosine is

$$(\mathbf{k}_1 - \mathbf{k}_2) \cdot \mathbf{r} = \frac{2\pi}{\lambda}[(l_1 - l_2)\,\hat{\mathbf{x}} + (m_1 - m_2)\,\hat{\mathbf{y}} + (n_1 - n_2)\,\hat{\mathbf{z}}] \cdot \mathbf{r} \tag{3.19}$$

Let $l_{12} = l_1 - l_2$, and similarly for m and n. Since the cosine is required to equal 1, the argument must be $2\pi p$, where p is an integer.

$$\frac{2\pi}{\lambda}[l_{12}\,x + m_{12}\,y + n_{12}\,z] = 2\pi p$$

$$l_{12}\,x + m_{12}\,y + n_{12}\,z = p\lambda \tag{3.20}$$

The same is true for the second and third terms in (3.18), and these are a system of equations:

$$\begin{aligned} l_{12}x + m_{12}y + n_{12}z &= p_1\lambda, \\ l_{13}x + m_{13}y + n_{13}z &= p_2\lambda, \\ l_{14}x + m_{14}y + n_{14}z &= p_3\lambda \end{aligned} \tag{3.21}$$

Note that the integers need not be the same for this condition to be true, so each is given an index, and $p_i = 0, \pm 1, \pm 2, ...$ Cramer's rule is used to find x, y, z. This technique expresses the solution by replacing one of the columns in the determinant of the coefficient matrix with the vector on the right, (p_1, p_2, p_3). This is true for an arbitrary number of unknowns,

as long as the solution is unique.

$$x = \Delta^{-1}\begin{vmatrix} p_1 & m_{12} & n_{12} \\ p_2 & m_{13} & n_{13} \\ p_3 & m_{14} & n_{14} \end{vmatrix}, \quad y = \Delta^{-1}\begin{vmatrix} l_{12} & p_1 & n_{12} \\ l_{13} & p_2 & n_{13} \\ l_{12} & p_3 & n_{14} \end{vmatrix}, \quad z = \Delta^{-1}\begin{vmatrix} l_{12} & m_{12} & p_1 \\ l_{13} & m_{13} & p_2 \\ l_{12} & m_{14} & p_3 \end{vmatrix}$$

where

$$\Delta = \begin{vmatrix} l_{12} & m_{12} & n_{12} \\ l_{13} & m_{13} & n_{13} \\ l_{12} & m_{14} & n_{14} \end{vmatrix} \tag{3.22}$$

This solution determines the locations of maximum interference between any four laser beams. Put in terms of an optical lattice, this determines the locations at which atoms will be trapped for red-detuned light. Changing p_j in each equation in (3.21) by 1, then, determines a translation from one optical lattice site to another. Hence, this solution defines the basis of the optical lattice. From (3.22), the basis vectors are determined:

$$\mathbf{a}_1 = \frac{\lambda}{\Delta}\left(\begin{vmatrix} m_{13} & n_{13} \\ m_{14} & n_{14} \end{vmatrix}, \begin{vmatrix} n_{13} & l_{13} \\ n_{14} & l_{14} \end{vmatrix}, \begin{vmatrix} l_{13} & m_{13} \\ l_{14} & m_{14} \end{vmatrix} \right),$$

$$\mathbf{a}_2 = \frac{\lambda}{\Delta}\left(\begin{vmatrix} m_{12} & n_{12} \\ m_{14} & n_{14} \end{vmatrix}, \begin{vmatrix} n_{12} & l_{12} \\ n_{14} & l_{14} \end{vmatrix}, \begin{vmatrix} l_{12} & m_{12} \\ l_{14} & m_{14} \end{vmatrix} \right),$$

$$\mathbf{a}_3 = \frac{\lambda}{\Delta}\left(\begin{vmatrix} m_{12} & n_{12} \\ m_{13} & n_{13} \end{vmatrix}, \begin{vmatrix} n_{12} & l_{12} \\ n_{13} & l_{13} \end{vmatrix}, \begin{vmatrix} l_{12} & m_{12} \\ l_{13} & m_{13} \end{vmatrix} \right) \tag{3.23}$$

This is the general solution for the interference of four plane waves, from which we can learn a few things about the nature of the optical lattice. The basis vectors are determined only by the geometry of the four wave vectors and their wavelength. Consequently, when we are after structures with multi-atom bases, we should find the nature of the basis is irrelevant to the beam geometry. For example, the geometry of the face-centered cubic optical lattice and the diamond lattice turn out to be identical, only they require different polarizations and power ratios to form the correct basis.

Using this result we can develop the optical lattice geometry of a selection of crystal structures discussed in Chapter 3. In principle, the beam geometry for any of the fourteen Bravais lattices in Table 2.1 can be determined, as demonstrated by Cai [16]. Here we summarize some of the results from these simulations, namely the cubic system. While the

Table 3.1

	$\mathbf{k}_1$	$\mathbf{k}_2$	$\mathbf{k}_3$	$\mathbf{k}_4$
sc	(1, 1, 1)	(-1, 1, 1)	(1, -1, 1)	(1, 1, -1)
fcc	(3, 3, 3)	(1, 1, 5)	(5, 1, 1)	(1, 5, 1)
bcc	(1, 1, 1)	(1, -1, -1)	(-1, 1, -1)	(-1, -1, 1)
diamond	(0, -2, -1)	(2, 0, 1)	(0, 2, -1)	(-2, 0, 1)

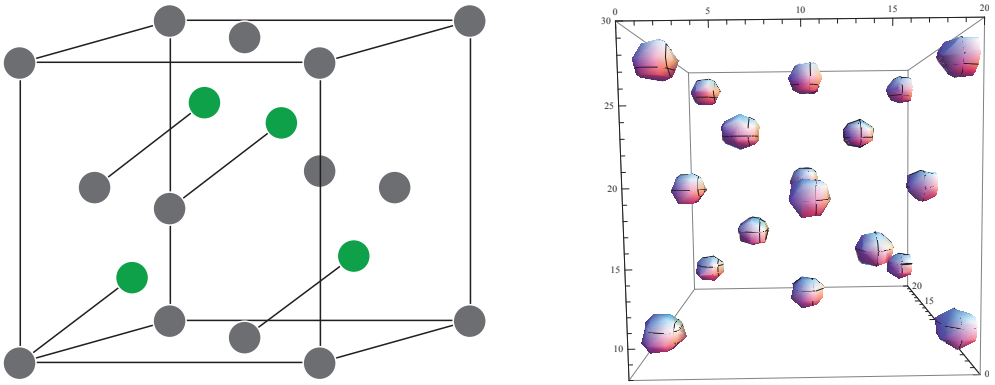

Figure 3.3: Left: an ideal cubic diamond crystal. This has the same geometry as the fcc lattice, but with a two atom basis. The second atom in the diamond basis is represented by a green lattice site here. Right: a computer model of the diamond optical lattice generated by a four-beam interference pattern. The MATHEMATICA code can be found in Appendix A.

mathematical calculations are not carried out here, the results are confirmed by simulating the intensity pattern in the Appendix. By working backwards from Δ in (3.22), the wavevectors of each beam, $\mathbf{k}_1, \mathbf{k}_2, \mathbf{k}_3, \mathbf{k}_4$, are found. The four wavevectors for the cubic system are tabulated in Table 3.1.

The Bravais lattice vectors are determined only by the geometric relationship of the four laser beams. The beam polarizations and amplitudes determine the basis of the optical lattice [18]. Optimizing these beam parameters has to do with reaching uniform contrast, i.e. the contribution of each beam is the same as the other three. This ensures the lattice will truly be a four-beam lattice. To optimize the amplitudes, the ratio of each pair of beams must contribute equally to the contrast. For polarizations, the orientations are optimized to maximize the contrast.

The four-beam geometry for the cubic diamond lattice is found following Toader [15]. The calculations for polarization and amplitude optimization are confirmed by generating a contour plot of the four-beam geometry, shown in Figure 3.3. The optimized amplitudes for the beam geometry listed in Table 3.1 are $\{E_1, E_2, E_3, E_4\} = \{A, B, B, B\}$ where $A/B = 1/\sqrt{17}$. The polarizations are parameterized by a rotation of $\mathbf{U}_i$ about $\mathbf{k}_i$. For the diamond lattice these are $\{\theta_1, \theta_2, \theta_3, \theta_4\} = \{350.4°, 244.3°, 105.7°, 16.1°\}$.[2]

[2]This analysis is a summary of the results of Cai [16] and Toader [15]. These approaches are surprisingly different, especially with respect to distinguishing between the direct and reciprocal lattices. Since the diamond is an fcc lattice with a two atom basis, we expect the diamond beam geometry to be the same as the fcc lattice; however, it is instead identical to the bcc beam geometry.

Chapter 4

Kapitza-Dirac scattering in a multi-dimensional optical lattice

A majority of the experimental work done for this project was the construction of the optical apparatus for the lattice beams. A four-beam optical lattice is realized by an apparatus that splits one beam to four. The incoming beam is produced by a titanium sapphire laser. Ideally, this apparatus would be constructed to produce each beam with stable intensity, and a precisely known linear polarization. In addition, we would like to be able to have active control over these parameters. This thesis sacrifices some of these precise controls for more practical solutions. After a summary of the relevant optics background, this chapter includes an overview of optical apparatus and some of the troubleshooting of the experimental implementation. In conclusion, some scattering images of multi-dimensional lattices are included.

4.1 One-to-four optical apparatus

The source of the lattice beams is a SolsTiS titanium sapphire (Ti:sapph) laser, which is a widely tunable, continuous wave narrow line width laser. The typical wavelength range available with the SolsTiS is roughly 670 nm to >1000 nm. The maximum output power is 5.6 Watts at 780 nm. Various optical elements are added to the sealed laser cavity to limit the number of oscillating cavity modes. The mechanical design of the laser ensures relatively high stability, but additional electronic servo locking systems reduce the laser rms linewidth to < 50 kHz. These elements, viz. a birefringent filter (BFR), a locking inter-cavity étalon, and cavity length PZT.

The laser wavelength can be tuned by rotating the BFR, which is used only for coarse adjustments. Extremely narrow linewidth is realized by adjusting the inter-cavity thin étalon spacing. Typically the output is single mode, but to eliminate any possibility of mode hopping the étalon has electronic servo locking, which locks to the nearest longitudinal mode. Once this is locked, even finer control over the cavity length is achieved with a long-throw PZT-mounted mirror. The narrowest possible linewidth is realized by a high stability, high finesse, reference cavity, to which the Ti:sapph is locked. These elements are responsible for the sub-50 kHz laser linewidth. All laser elements are controlled by computer via Ethernet connection. This, in principle, enables us to manipulate the wavelength of the Ti:sapph remotely. With finesse of this caliber, we are able to tune the wavelength of the lattice beams to within one ten-thousandth of a nanometer. This precision is extremely important when installing the lattice beams at the experiment, as described later in this chapter.

About 30 mW of Ti:sapph power is coupled to a polarization maintaining fiber and delivered to the experiment, where it is collimated and split four ways. The output power is typically 20 mW, which is more than adequate. The input power is controlled by an acousto-optic modulator. A zero-order one-half wave plate controls the polarization orientation such that the output polarization does not drift significantly, as this causes massive power fluctuations in the four lattice beams at the experiment.

The collimated Ti:sapph beam (spot size roughly 1 mm) moves through a series of polarizing beam splitters and four beam paths are focused into individual fibers sent to the experiment. The intensity ratio of the beamsplitters are determined by zero-order half-wave plates preceding each cube. Intensity control is passively achieved for three lattice beams, and the intensity of the fourth special beam is set up for potential servo control, described later on in this section. The optical diagram is shown in Figure 4.1.

Before coupling, each beam passes through a zero-order half-wave plate, which is mounted on a rotation stage cage mount. This allows for passive control over the polarization before it is coupled. The beam is then focused into the fiber launcher with an aspherical lens. The ideal focal length is found using

$$f = \frac{\pi D(MFD)}{4\lambda} \tag{4.1}$$

where D is the beam diameter, and MFD is the mode field diameter of the fiber. ($MFD = 4.9\mu$m at 780 nm.) The closest commercially available focal length is 7.50 mm. The fiber launcher is mounted in a z-translation stage cage mount to optimize the distance from the aspherical lens. In this setup, any x, y adjustments are made with the mirror mounts alone, which speeds up the coupling process. The coupling efficiency for all beams is well over 50%,

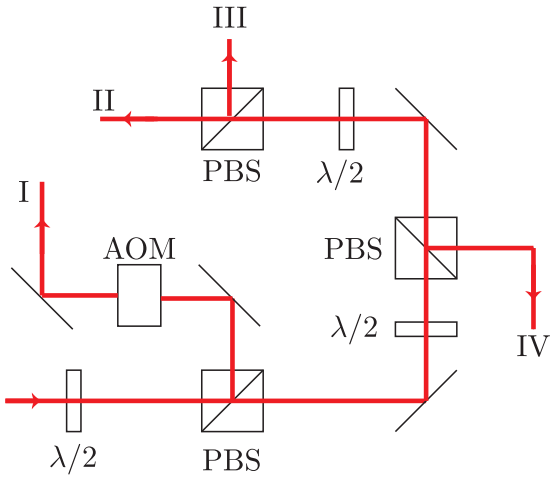

Figure 4.1: A simplified diagram of the optical apparatus. Light from the Ti:sapph input fiber (bottom left) is collimated and split four-ways to be sent to the experiment. All $\lambda/2$ wave plates are mounted on rotation stages such that the light transmitted through each PBS can be varied. Beam I is the "special" beam, which is set up to support intensity servo control by sending negative feedback to the AOM with a pick-off optic and a high-speed photodetector. Not included in this diagram is the focusing and fiber coupling apparatus for each of the four beams, which is shown in Figure 4.2.

which is more than adequate for this type of experiment.

The beams are focused into polarization maintaining (PM) fibers. These have stress birefringence that forces light polarized along the orthogonal axes of the fiber to travel at different speeds. The output polarization is determined by how much light is projected onto each axis. The next section outlines polarization stabilization techniques, but "polarization maintaining" fiber is an extremely misleading title, as this is one of the biggest experimental challenges here.

On the output of the fiber the beam is collimated and sent to the experiment. The collimating aspherical lens has a slightly shorter focal length ($f = 6.44$ mm) than the coupling lens to increase the spot size to roughly 1.6 mm. The fiber launcher and collimating lens are mounted in an adjustable-length 1/2 inch lens tube, attached to a threaded kinematic mirror mount, as shown in Figure 4.3. The mount can be translated along the horizontal or vertical direction once the mount is roughly in place. The adjustable-length lens tube is intended to control the angular orientation of the fiber launcher, which should—in principle—provide mechanical control over output polarization. The collimation apparatus in Figure 4.3 is mounted on 1/2 inch post which provides tip-tilt control for coarse alignment. This is mounted to a 16 inch post which is clamped to the optical table.

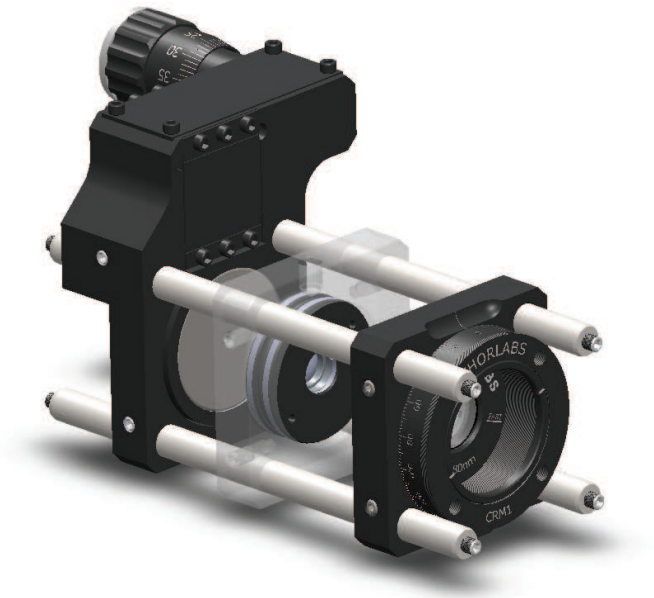

Figure 4.2: A rendering of the cage-mounted fiber coupling apparatus. From front to back: a zero-order half-wave plate mounted in a rotation stage; an aspherical lens of focal length 7.5 mm mounted in an adapter and cage plate; the fiber launcher mounted in a z-translation stage. Not shown is an additional cage plate which is needed to mount the cage system to the optical breadboard. This is a 30 mm cage system suitable for 1 inch optics, and the length of the cage rods is 4 inches. Source: Thorlabs, Inc.

4.2 Polarization maintenance

The crucial parameters of this experiment are the intensities and polarizations of each beam. Specifically, the ratios of the four individual beam intensities, and the polarization angles with respect to $\mathbf{U}_i$. One of the tricky experimental limitations is ensuring the polarization of each beam hits the "good" axis of the fiber. If the polarization is not aligned with this axis when coupled into a polarization maintaining (PM) fiber, the output polarization will rotate. This is obviously an issue given the specificity of the polarization angles found in the previous chapter.

Rectifying this process is not simple. This phenomenon arrises in two different ways. First, the fiber delivering the Ti:sapph light to the one-to-four setup must have the correct orientation. The second is the polarization orientations of the beams at the experiment itself. A PM fiber induces a difference in the speed of light along the perpendicular axes (the fast axis and the slow axis). If the output polarization rotates upon reaching the first PBS, the transmission ratio will fluctuate and the power along each path will change. For a perfectly

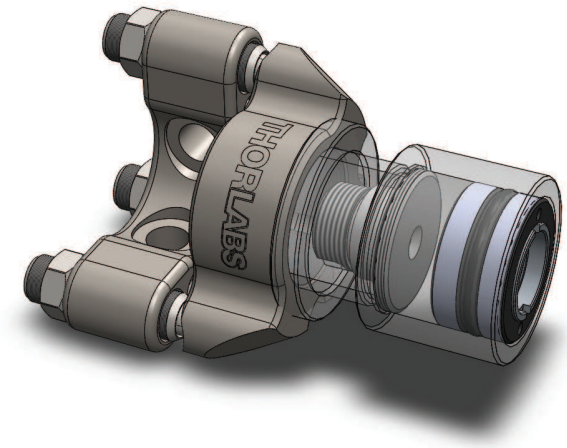

Figure 4.3: 3D rendering of the collimation apparatus. Inside the adjustable-length lens tube, the fiber launcher and the 0.5 inch lens adapter are held fixed a focal length apart. The lens tube is free to rotate about the threaded mirror mount, and can be fixed in place by the external retaining ring. Source: Thorlabs, Inc.

linearly polarized beam an angle θ from the fiber launcher's slow axis, the output power is limited by the extinction ratio:

$$ER \leq 10 \log_{10}(\tan^2 \theta) \tag{4.2}$$

In order to achieve reasonable extinction ratios—above 20 dB—the misalignment can be no more than 6°. For extinction ratios above 30 dB it must be within 1.8° [19]. The extinction ratio describes the loss through the fiber, but this accompanies a rotating output polarization that causes large fluctuations between transmission and reflection in a PBS. So polarization stability to even within ±1° is a tall order without any automated servo control. At best, the PM fibers limit the polarization output from wandering more than ±6°, so the 20 dB extinction ratio is within reach. This problem is rectified by adding a half-wave plate preceding the focusing lens. The PM fiber is truly "polarization maintaining" when the half-wave plate changes the polarization such that all light travels along the slow axis of the fiber. The heart of this challenge is determining whether the input polarization is aligned within such a small range of the slow axis.

An additional polarization-related issue arrises at the experiment. The polarization can be set to any angle by adding a half-wave plate, but in this experiment we attempt to achieve this mechanically. This is done by allowing the fiber launcher and collimating lens to rotate together, such that the orientation of the slow axis is free to rotate around **k** without distorting the spot size. The lens tube containing the collimation optics is fixed to a mount with a washer. Unfortunately, this all becomes a moot point if the orientation of the wave plate prior to the focusing lens is not at the correct angle, as this results in somewhat random fluctuations in the output polarization.

Effectively solving this problem involves complicated servo control that monitors the extinction ratio and the orientation of the wave plate. An efficient method for finding the good orientation of the wave plate involves monitoring the birefringence of the output beam. In order to optimize the angle the output light must be collimated and pass through a polarizing optic (we use a PBS), and the transmitted power is measured and the signal is displayed on an oscilloscope. At a random polarization angle the signal fluctuates over a period on the order of tens of seconds, depending on the length of the fiber. Removing the polarizing optic confirms the fluctuations are a result of changes in the output polarization and not just background fluctuations, e.g. drift in the Ti:sapph power, poor coupling, etc.

With the optic back in place, the output signal is monitored while the fiber is perturbed. We have found the most effective method is to coil the fiber and heat a section of it by holding it in hand. This "squeeze test" will result in a remarkably clean periodic oscillation in the output signal, which is caused by the built-in birefringence in the PM fiber. The optimal orientation of the input half-wave plate is found iteratively using this method. At the optimal angle the input light travels along only the slow axis of the fiber and the squeeze test has minimal effect.

While this method is effective to a good degree, it is neither time-efficient nor can it reach the precision of automated processes. If highly determined polarizations are experimentally required, these are certainly worth-while investments. With larger time allowance, this thesis would explore some type of servo control for the beam polarizations. The most viable solution would be managing the polarization after it is collimated at the experiment using a series of polarizers and negative feedback to manage the transmission power. This approach would abandon the use of overly ambitious PM fibers. The main limitation in this case would be space; adding more optical elements after collimation can be bulky, and airspace at the experiment is valuable.

4.3 Experimental synopsis

The geometry of the beam orientations is limited by preexisting lab infrastructure, making the realization of any specific lattice geometry unrealistic. Optical access to the science chamber is restricted to a range of angles below roughly 20° from horizontal. Even so, the four-beam geometry roughly resembles the fcc geometry.

Aligning the lattice is done in three stages. The first is by estimating the alignment such that it is roughly positioned at the center of the chamber, which in this experiment conveniently corresponds to the location of the MOT. The Ti:sapph is tuned so it is on-resonance with the $F = 2 \rightarrow F' = 3$ transition ($\lambda = 780.2462$ nm). We can determine whether the lattice beam is positioned correctly by fine tuning the mirror mount and monitoring perturbations in the image of the MOT. Slight perturbations can be seen if the laser is slightly detuned, and if the Ti:sapph is on-resonance the MOT will be completely destroyed by the lattice beam.

After a beam is aligned such that it destroys a MOT, we switch to a MOT generated with the magnetic trap coils. The MOT coils can provide a magnetic field of only 15 G/cm, so next we can repeat this procedure for a MOT with tighter confinement of 200 G/cm, ramped up from 75 G/cm. Aligning the beams with the center of the tightly-confined MOT should ensure the beam will be aligned with the location of the condensate to within 100 μm, the distance the atoms are displaced when they are loaded into the dipole trap. Since the spot size of each lattice beam is ~ 1.6 mm, we expect this to be trivial once the beam is aligned with the tightly confined MOT.

The next step is pulsing the lattice once the cloud becomes critical in the dipole trap. At this stage the light is no longer on-resonance, as the atoms have been depumped to $F = 1$ before the loading into the magnetic trap. By trial-and-error the beam orientation is finely adjusted such that perturbations in the BEC are maximized. (For frequencies close to resonance this should result in smaller clouds.) Without systematic control over the power ratios of the beams, these are passively tuned by adjusting half-wave plates in the one-to-four apparatus such that the output power of each beam is roughly equal. Each beam has 5 – 10 mW.

Once the beams are aligned with the BEC we can start looking for scattering in the TOF by pulsing multiple beams. To lower the scattering rate the Ti:sapph is detuned further to 780.260 nm. To start, we optimize the pulse length for each pair of beams. These produce two-beam one-dimensional optical lattices, so the BEC splits into multiple collinear clouds along $\mathbf{k}_i - \mathbf{k}_j$ in momentum space. At an average output power of 6 mW in each beam,

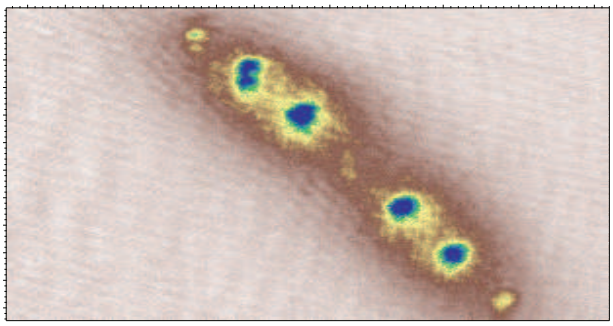

Figure 4.4: Kapitza-Dirac scattering in a two beam optical lattice pulsed for 1 μs. Both beams had 2 mW of power.

the pulse lengths needed to see well-populated higher order clouds is 2 μs. There is a clear lower limit to experimentally possible pulse durations at roughly 1 μs, which results from a sluggish response in the AOM.[1] This is an easy issue to work around by detuning further from resonance. This lowers the scattering rate so the pulse duration can be longer. In this one-dimensional case, the separation between lattice orders $2v_{rec}t$, or

$$d = \frac{2\,\hbar k\, t_{TOF}}{m} \tag{4.3}$$

where m is the mass of rubidium. Typical TOF lengths $t_{TOF} = 15$ ms. Since the imaging axis is not orthogonal to the lattice, we see the projection of this separation, $d\cos\theta$.

Adding a third lattice beam increases the complexity of the TOF image. For three beams, the BEC splits into coplanar clouds. The orientation of the plane is determined by two of the three $\mathbf{k}_i - \mathbf{k}_j$ combinations, as discussed in Chapter 4. Again, the pulse length is optimized around 2 μs to see well-populated higher orders.

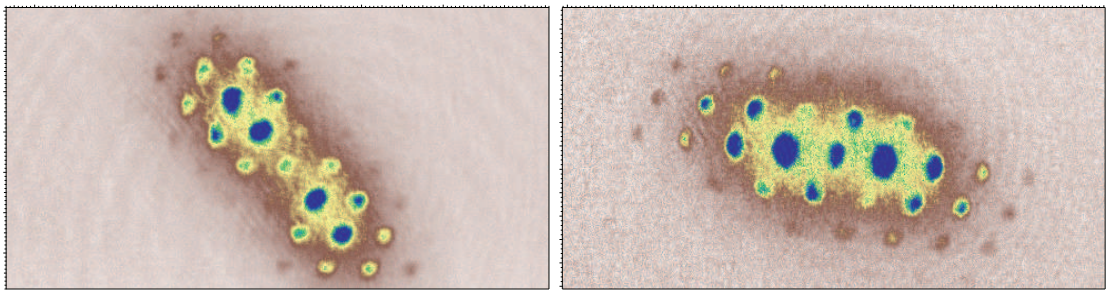

Figure 4.5: Kapitza-Dirac scattering in a three-beam optical lattice. Two of the three lattice beams are common to both lattices. Both lattices are pulsed for 1 μs.

[1] This limit is due to the speed of sound of phonon propagation in the AOM crystal.

Some absorption images are taken for a four-beam optical lattice, but it is difficult to interpret a three-dimensional image along only one imaging axis, as shown in Figure 4.6. For three beams we see a plane projected onto the imaging axis, so some of the image is more in focus and this is what is interpreted as depth. A cloud expanding in three dimensions is too complex to fully understand without two or more images of the TOF. These can be projected in two dimensions and then divided themselves to render a three-dimensional absorption plot.

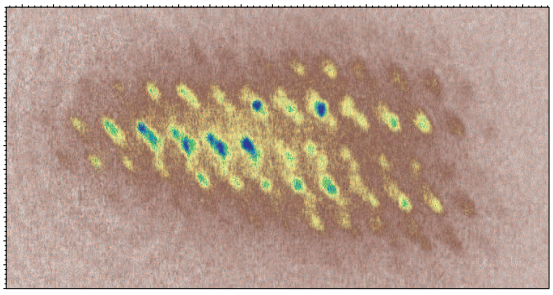

Figure 4.6: A four-beam three-dimensional optical lattice pulsed for 1 μs. The cloud is clearly moving in all directions, making this a difficult image to fully understand.

4.4 Outlook & improvements

At the onset of this thesis, the preliminary goal was to load the BEC into an optical lattice in the diamond configuration. The first half of the project was mostly computational simulations of interference patterns for various beam geometries. Once the solution for a lattice of this complexity was found, it became clear that this requires precise control over too many parameters to be experimentally realistic. We revised the experimental goal to seeing some arbitrary four-beam optical lattice, with some type of control over the beam polarization states.

Once the one-to-four optical apparatus was completed and we began aligning the lattice beams with the experiment we ran into problems with on-resonant light leaking through the zeroth order of an AOM from an atom interferometry experiment. This had not been a problem until the Ti:sapph was tuned to resonance to align our lattice beams with the MOT. The BEC machine would stop producing condensates after working well for the first half hour of operation. This symptom seemed like it was related to the quadrupole trap, potentially as a result of some unwanted electrical connections. Fortunately, the root of the problem was discovered and resolved in time to spend a few days loading the optical lattice;

however, we were not able to observe the effect of the polarization states. Especially after the effort to stabilize polarizations, this is an interesting parameter that would be worth investigating.

Another obvious next step is working towards understanding the real-space geometry of this optical lattice. An ideal follow up project would be simulating the beam geometry to get an understanding of the scattering images. This requires only passive knowledge of the lattice beam powers, and a rough estimation of the polarization state. The optical apparatus is also set up to have active servo control on one of the four lattice beams, though this was not included in this experiment.[2]

[2]The zeroth order must be the coupled beam, as the diffracted orders have a different frequency and will not work for pulsed scattering.

Appendices

Appendix A

Diamond cubic lattice

```
λ = 1;
k = 4;

xhat = {1, 0, 0};
yhat = {0, 1, 0};
zhat = {0, 0, 1};

r[x_, y_, z_] := {x, y, z};
```

Diamond cubic wavevectors

```
k0 = Normalize[{0, -2, -1 }];
k1 = Normalize[{2, 0, 1}];
k2 = Normalize[{0, 2, -1}];
k3 = Normalize[{-2, 0, 1}];

Norm[k0 - k1] // N
Norm[k0 - k2] // N
Norm[k0 - k3] // N
Norm[k1 - k2] // N
Norm[k1 - k3] // N
Norm[k2 - k3] // N
```

```
1.54919

1.78885

1.54919

1.54919

1.78885

1.54919
```

3D plot of propagation vectors without polarizations. Arrows pointing backwards...

```
ParametricPlot3D[{{k1} * u, {k2} * u, {k3} * u, {k4} * u}, {u, 0, 1}] /. Line → Arrow
```

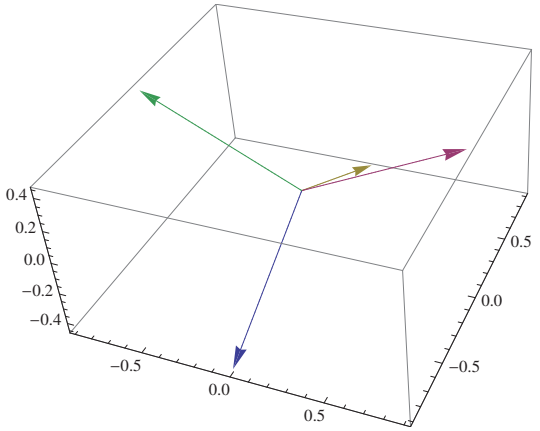

Define k, R, U triads, and a 3D plot confirming orthogonality...

```
R0 = Normalize[k0 × zhat];
R1 = Normalize[k1 × zhat];
R2 = Normalize[k2 × zhat];
R3 = Normalize[k3 × zhat];

U0 = Normalize[R0 × k0];
U1 = Normalize[R1 × k1];
U2 = Normalize[R2 × k2];
U3 = Normalize[R3 × k3];
```

```
ParametricPlot3D[{U2, k2, R2} * u, {u, 0, .5}] /. Line → Arrow
```

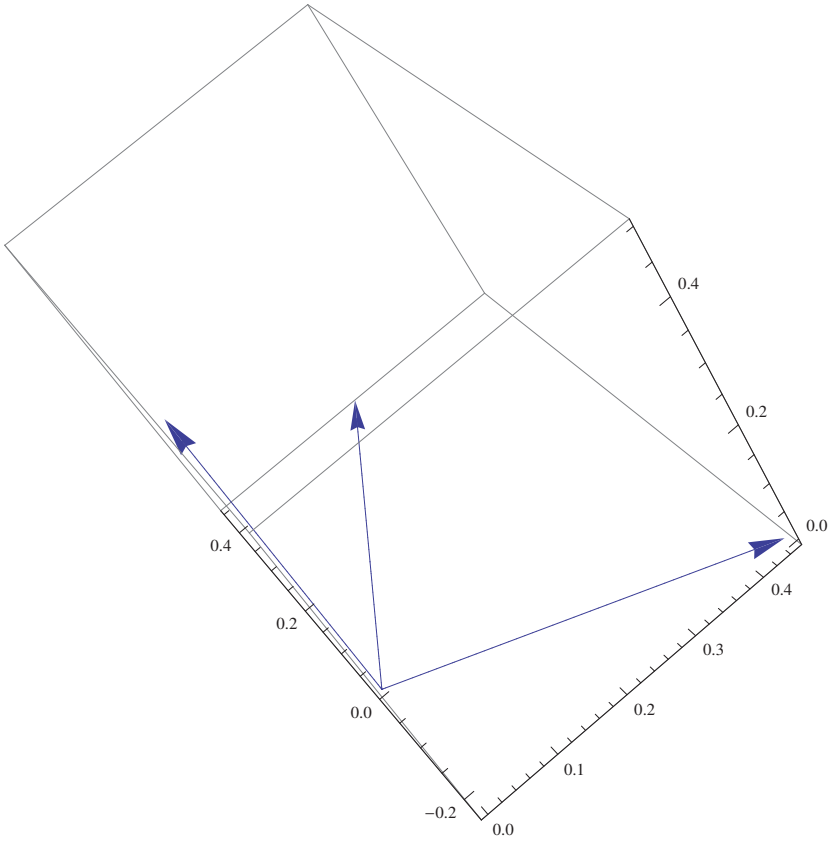

Polarization vectors defined as a rotation from the U vector about k. Angles found by Toader (see bibliography)...

```
e0 = RotationMatrix[350.4 Degree, k0].U0;
e1 = RotationMatrix[244.3 Degree, k1].U1;
e2 = RotationMatrix[105.7 Degree, k2].U2;
e3 = RotationMatrix[16.1 Degree, k3].U3;
```

Define 4 beams, Etotal, and the Intensity . . .

```
Beam0[x_, y_, z_, E1_] := E1 Exp[I k k0 . r[x, y, z]] e0
Beam1[x_, y_, z_, E2_] := E2 Exp[I k k1 . r[x, y, z]] e1
Beam2[x_, y_, z_, E3_] := E3 Exp[I k k2 . r[x, y, z]] e2
Beam3[x_, y_, z_, E4_] := E4 Exp[I k k3 . r[x, y, z]] e3


Etot[x_, y_, z_, E1_, E2_, E3_, E4_] :=
  Beam0[x, y, z, E1] + Beam1[x, y, z, E2] + Beam2[x, y, z, E3] + Beam3[x, y, z, E4];

Intensity[x_, y_, z_, E1_, E2_, E3_, E4_] :=
 Conjugate[Etot[x, y, z, E1, E2, E3, E4]].Etot[x, y, z, E1, E2, E3, E4]

Intensity[x, y, z, 1, 1, 1, 1]  // ComplexExpand // Simplify // Chop
```

$$-0.000217007\,\text{Cos}\left[\frac{16\,x}{\sqrt{5}}\right]+0.000920631\,\text{Cos}\left[\frac{16\,y}{\sqrt{5}}\right]+$$
$$1.\,\text{Cos}\left[\frac{8\,x-4\,z}{\sqrt{5}}\right]^2+0.344188\,\text{Cos}\left[\frac{8\,x-4\,z}{\sqrt{5}}\right]\text{Cos}\left[\frac{8\,y-4\,z}{\sqrt{5}}\right]+1.\,\text{Cos}\left[\frac{8\,y-4\,z}{\sqrt{5}}\right]^2+$$
$$0.343073\,\text{Cos}\left[\frac{8\,y-4\,z}{\sqrt{5}}\right]\text{Cos}\left[\frac{4\,(2\,x+z)}{\sqrt{5}}\right]+1.\,\text{Cos}\left[\frac{4\,(2\,x+z)}{\sqrt{5}}\right]^2+$$
$$1.41447\,\text{Cos}\left[\frac{8\,x-4\,z}{\sqrt{5}}\right]\text{Cos}\left[\frac{4\,(2\,y+z)}{\sqrt{5}}\right]-1.41411\,\text{Cos}\left[\frac{4\,(2\,x+z)}{\sqrt{5}}\right]\text{Cos}\left[\frac{4\,(2\,y+z)}{\sqrt{5}}\right]+$$
$$1.\,\text{Cos}\left[\frac{4\,(2\,y+z)}{\sqrt{5}}\right]^2+1.\,\text{Sin}\left[\frac{8\,x-4\,z}{\sqrt{5}}\right]^2-0.344188\,\text{Sin}\left[\frac{8\,x-4\,z}{\sqrt{5}}\right]\text{Sin}\left[\frac{8\,y-4\,z}{\sqrt{5}}\right]+$$
$$1.\,\text{Sin}\left[\frac{8\,y-4\,z}{\sqrt{5}}\right]^2+0.343073\,\text{Sin}\left[\frac{8\,y-4\,z}{\sqrt{5}}\right]\text{Sin}\left[\frac{4\,(2\,x+z)}{\sqrt{5}}\right]+$$
$$1.\,\text{Sin}\left[\frac{4\,(2\,x+z)}{\sqrt{5}}\right]^2+1.41447\,\text{Sin}\left[\frac{8\,x-4\,z}{\sqrt{5}}\right]\text{Sin}\left[\frac{4\,(2\,y+z)}{\sqrt{5}}\right]+$$
$$1.41411\,\text{Sin}\left[\frac{4\,(2\,x+z)}{\sqrt{5}}\right]\text{Sin}\left[\frac{4\,(2\,y+z)}{\sqrt{5}}\right]+1.\,\text{Sin}\left[\frac{4\,(2\,y+z)}{\sqrt{5}}\right]^2$$

```
% // N
```

```
-0.000217007 Cos[7.15542 x] + 0.000920631 Cos[7.15542 y] + 1. Cos[0.447214 (8. x - 4. z)]^2 +
 0.344188 Cos[0.447214 (8. x - 4. z)] Cos[0.447214 (8. y - 4. z)] +
 1. Cos[0.447214 (8. y - 4. z)]^2 + 0.343073 Cos[0.447214 (8. y - 4. z)] Cos[1.78885 (2. x + z)] +
 1. Cos[1.78885 (2. x + z)]^2 + 1.41447 Cos[0.447214 (8. x - 4. z)] Cos[1.78885 (2. y + z)] -
 1.41411 Cos[1.78885 (2. x + z)] Cos[1.78885 (2. y + z)] + 1. Cos[1.78885 (2. y + z)]^2 +
 1. Sin[0.447214 (8. x - 4. z)]^2 - 0.344188 Sin[0.447214 (8. x - 4. z)] Sin[0.447214 (8. y - 4. z)] +
 1. Sin[0.447214 (8. y - 4. z)]^2 + 0.343073 Sin[0.447214 (8. y - 4. z)] Sin[1.78885 (2. x + z)] +
 1. Sin[1.78885 (2. x + z)]^2 + 1.41447 Sin[0.447214 (8. x - 4. z)] Sin[1.78885 (2. y + z)] +
 1.41411 Sin[1.78885 (2. x + z)] Sin[1.78885 (2. y + z)] + 1. Sin[1.78885 (2. y + z)]^2
```

Some contour plots in the x-y plane...

```
ContourPlot[Intensity[x, y, .375, 1 / Sqrt[17], 1, 1, 1],
 {x, -2, 2}, {y, -2, 2}, Mesh → Full, ColorFunction → "GrayTones"]
```

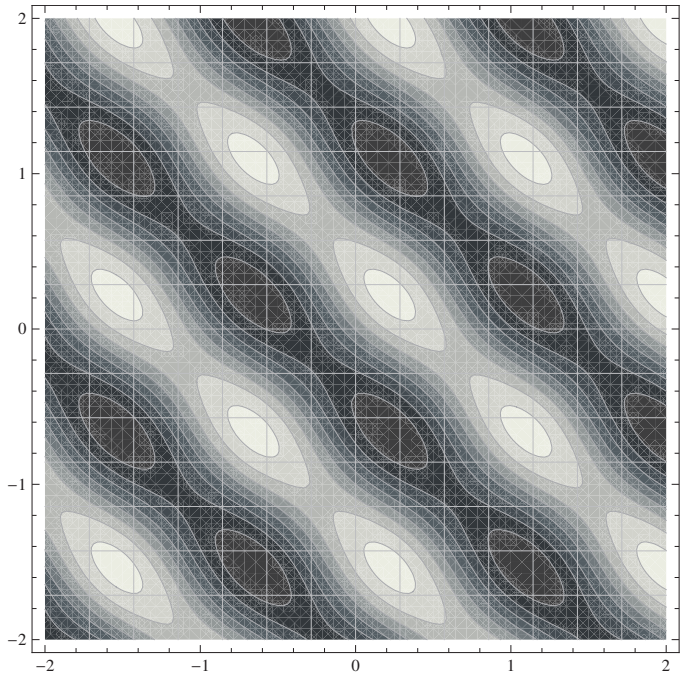


```
graph1 = ContourPlot[Intensity[x, y, 0, 1, 1, 1, 1],
    {x, 0, 3}, {y, 0, 3}, Mesh → Full, ColorFunction → "GrayTones"];
graph2 = ContourPlot[Intensity[x, y, 1 / 4, 1, 1, 1, 1], {x, 0, 3},
    {y, 0, 3}, Mesh → Full, ColorFunction → "GrayTones"];
graph3 = ContourPlot[Intensity[x, y, 1 / 2, 1, 1, 1, 1], {x, 0, 3},
    {y, 0, 3}, Mesh → Full, ColorFunction → "GrayTones"];
graph4 = ContourPlot[Intensity[x, y, 3 / 4, 1, 1, 1, 1], {x, 0, 3},
    {y, 0, 3}, Mesh → Full, ColorFunction → "GrayTones"];

GraphicsGrid[{{graph1, graph2}, {graph3, graph4}}]
```

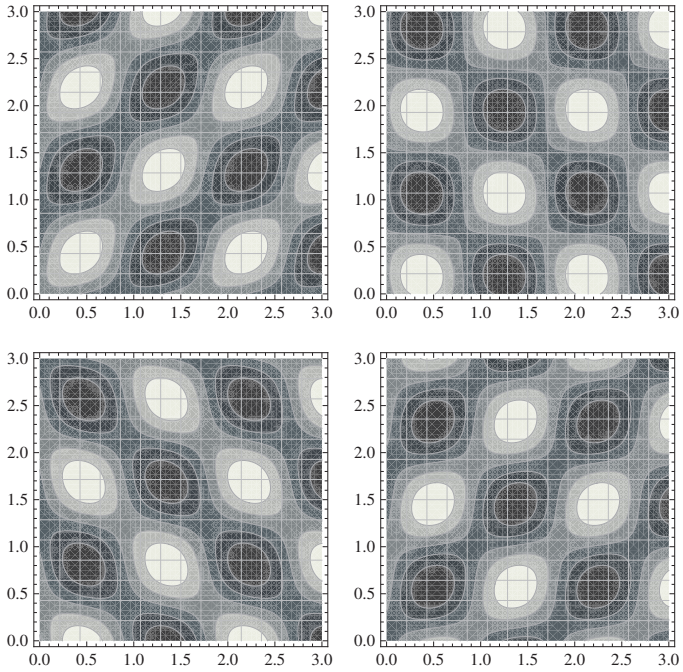


```
g = 1.7;
```

3D contour plot of interference pattern. The table speeds up the calculation by a factor of 10. Contour size chosen for the clearest visual the diamond lattice geometry.

```
ack = Table[Intensity[xi, yi, zi, 1 / Sqrt[17], 1, 1, 1],
    {xi, -g, g, .1}, {yi, -g, g, .1}, {zi, -g, g, .1}];
ListContourPlot3D[ack, Contours → {2.2}, PlotRange → {{0, 20}, {0, 20}, {8, 30}}]
```

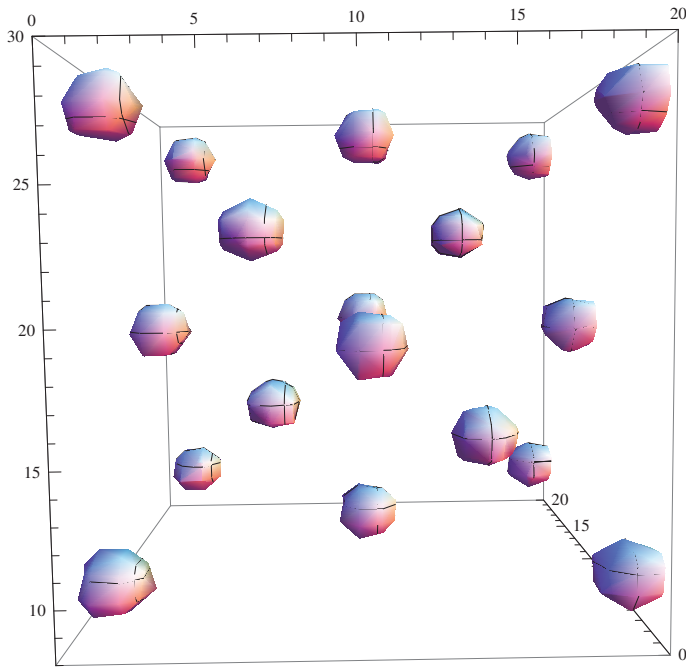
0
5
10
15
20
30
25
20
15
10
20
15
0

Appendix B

Body-centered cubic lattice

```
λ = 1;
k = 4;

xhat = {1, 0, 0};
yhat = {0, 1, 0};
zhat = {0, 0, 1};
r[x_, y_, z_] := {x, y, z};
```

Body-centered cubic wavevectors & polarizations...

```
k1 = {1, 1, 1};
k2 = {1, -1, -1};
k3 = {-1, 1, -1};
k4 = {-1, -1, 1};

e1 = {.816497, -.408248, -.408248};
e2 = {.816497, .408248, .408248};
e3 = {0, .707107, .707107};
e4 = e3;
```

3D plot of propagation vectors without polarizations. Arrows pointing backwards...

```
ParametricPlot3D[{{k1} * u, {k2} * u, {k3} * u, {k4} * u}, {u, 0, 1}] /. Line → Arrow
```

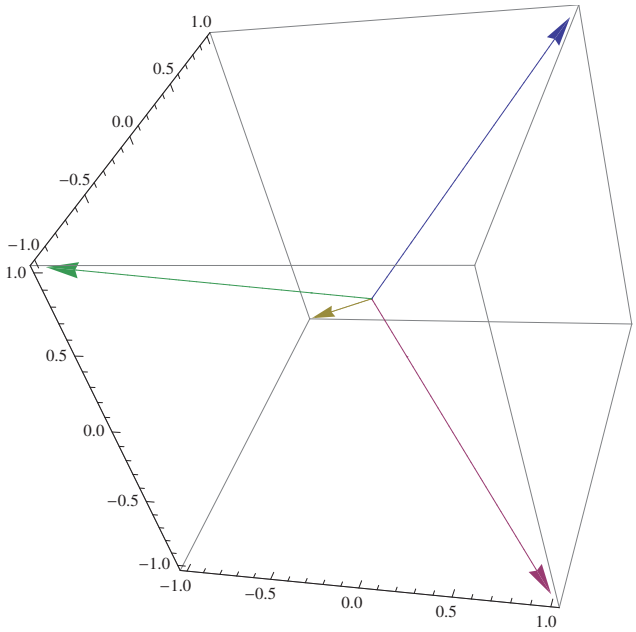


```
ParametricPlot3D[{{k1, e1} * u, {k2, e2} * u, {k3, e3} * u, {k4, e4} * u}, {u, 0, 1}] /.
 Line → Arrow
```

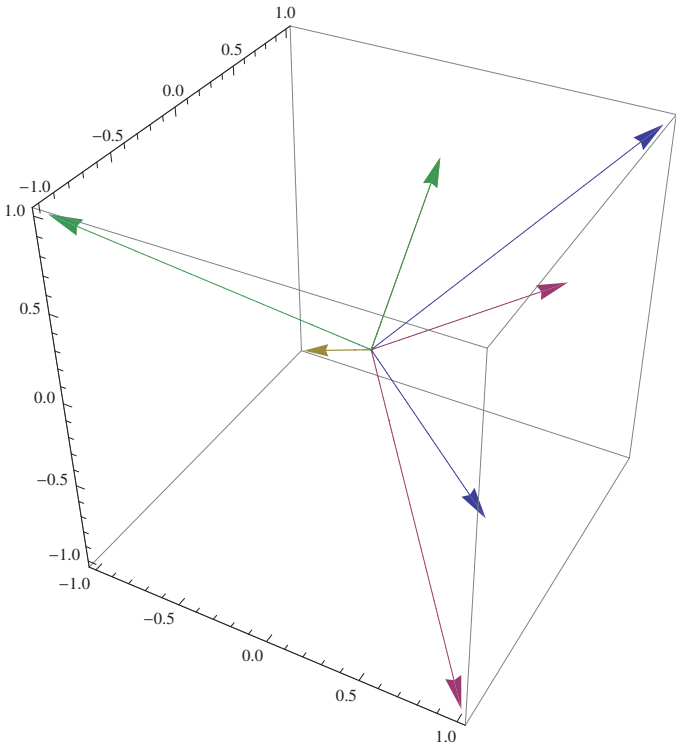


```
k1 = Normalize[k1];
k2 = Normalize[k2];
k3 = Normalize[k3];
k4 = Normalize[k4];
```

Define field for each of the four beams, the total E field, and the intensity...

```
Beam1[x_, y_, z_, E1_] := E1 Exp[I k k1 . r[x, y, z]] e1
Beam2[x_, y_, z_, E2_] := E2 Exp[I k k2 . r[x, y, z]] e2
Beam3[x_, y_, z_, E3_] := E3 Exp[I k k3 . r[x, y, z]] e3
Beam4[x_, y_, z_, E4_] := E4 Exp[I k k4 . r[x, y, z]] e4
```

```
Etot[x_, y_, z_, E1_, E2_, E3_, E4_] :=
  Beam1[x, y, z, E1] + Beam2[x, y, z, E2] + Beam3[x, y, z, E3] + Beam4[x, y, z, E4];
```

```
Intensity[x_, y_, z_, E1_, E2_, E3_, E4_] :=
 Conjugate[Etot[x, y, z, E1, E2, E3, E4]].Etot[x, y, z, E1, E2, E3, E4]
```

```
Intensity[x, y, z, 1, 1, 1, 1]  // ComplexExpand // Simplify // Chop
```

$$0.634075 \cos\left[\frac{16\,(x-y)}{3\sqrt{3}}\right] + 0.599128 \cos\left[\frac{16\,(x-z)}{3\sqrt{3}}\right] + 0.762418 \cos\left[\frac{16\,(y-z)}{3\sqrt{3}}\right] +$$
$$0.9998 \cos\left[\frac{4\,(x+y+z)}{\sqrt{3}}\right]^2 + 1.49691 \cos\left[\frac{4\,(x+y+z)}{\sqrt{3}}\right] \cos\left[\frac{4\,(5x+y+z)}{3\sqrt{3}}\right] +$$
$$0.907213 \cos\left[\frac{4\,(5x+y+z)}{3\sqrt{3}}\right]^2 + 0.634075 \cos\left[\frac{8\,(3x+3y+z)}{3\sqrt{3}}\right] +$$
$$1.85778 \cos\left[\frac{4\,(x+y+z)}{\sqrt{3}}\right] \cos\left[\frac{4\,(x+5y+z)}{3\sqrt{3}}\right] + 1.00016 \cos\left[\frac{4\,(x+5y+z)}{3\sqrt{3}}\right]^2 +$$
$$0.599128 \cos\left[\frac{8\,(3x+y+3z)}{3\sqrt{3}}\right] + 1.85817 \cos\left[\frac{4\,(x+y+z)}{\sqrt{3}}\right] \cos\left[\frac{4\,(x+y+5z)}{3\sqrt{3}}\right] +$$
$$1.00001 \cos\left[\frac{4\,(x+y+5z)}{3\sqrt{3}}\right]^2 + 0.762418 \cos\left[\frac{8\,(x+3\,(y+z))}{3\sqrt{3}}\right] +$$
$$0.9998 \sin\left[\frac{4\,(x+y+z)}{\sqrt{3}}\right]^2 + 1.49691 \sin\left[\frac{4\,(x+y+z)}{\sqrt{3}}\right] \sin\left[\frac{4\,(5x+y+z)}{3\sqrt{3}}\right] +$$
$$0.907213 \sin\left[\frac{4\,(5x+y+z)}{3\sqrt{3}}\right]^2 + 1.85778 \sin\left[\frac{4\,(x+y+z)}{\sqrt{3}}\right] \sin\left[\frac{4\,(x+5y+z)}{3\sqrt{3}}\right] +$$
$$1.26815 \sin\left[\frac{4\,(5x+y+z)}{3\sqrt{3}}\right] \sin\left[\frac{4\,(x+5y+z)}{3\sqrt{3}}\right] + 1.00016 \sin\left[\frac{4\,(x+5y+z)}{3\sqrt{3}}\right]^2 +$$
$$1.85817 \sin\left[\frac{4\,(x+y+z)}{\sqrt{3}}\right] \sin\left[\frac{4\,(x+y+5z)}{3\sqrt{3}}\right] + 1.19826 \sin\left[\frac{4\,(5x+y+z)}{3\sqrt{3}}\right] \sin\left[\frac{4\,(x+y+5z)}{3\sqrt{3}}\right] +$$
$$1.52484 \sin\left[\frac{4\,(x+5y+z)}{3\sqrt{3}}\right] \sin\left[\frac{4\,(x+y+5z)}{3\sqrt{3}}\right] + 1.00001 \sin\left[\frac{4\,(x+y+5z)}{3\sqrt{3}}\right]^2$$

```
% // N
```

```
0.634075 Cos[3.0792 (x - 1. y)] + 0.599128 Cos[3.0792 (x - 1. z)] + 0.762418 Cos[3.0792 (y - 1. z)] +
 0.9998 Cos[2.3094 (x + y + z)]^2 + 1.49691 Cos[2.3094 (x + y + z)] Cos[0.7698 (5. x + y + z)] +
 0.907213 Cos[0.7698 (5. x + y + z)]^2 + 0.634075 Cos[1.5396 (3. x + 3. y + z)] +
 1.85778 Cos[2.3094 (x + y + z)] Cos[0.7698 (x + 5. y + z)] + 1.00016 Cos[0.7698 (x + 5. y + z)]^2 +
 0.599128 Cos[1.5396 (3. x + y + 3. z)] + 1.85817 Cos[2.3094 (x + y + z)] Cos[0.7698 (x + y + 5. z)] +
 1.00001 Cos[0.7698 (x + y + 5. z)]^2 + 0.762418 Cos[1.5396 (x + 3. (y + z))] +
 0.9998 Sin[2.3094 (x + y + z)]^2 + 1.49691 Sin[2.3094 (x + y + z)] Sin[0.7698 (5. x + y + z)] +
 0.907213 Sin[0.7698 (5. x + y + z)]^2 + 1.85778 Sin[2.3094 (x + y + z)] Sin[0.7698 (x + 5. y + z)] +
 1.26815 Sin[0.7698 (5. x + y + z)] Sin[0.7698 (x + 5. y + z)] +
 1.00016 Sin[0.7698 (x + 5. y + z)]^2 + 1.85817 Sin[2.3094 (x + y + z)] Sin[0.7698 (x + y + 5. z)] +
 1.19826 Sin[0.7698 (5. x + y + z)] Sin[0.7698 (x + y + 5. z)] +
 1.52484 Sin[0.7698 (x + 5. y + z)] Sin[0.7698 (x + y + 5. z)] + 1.00001 Sin[0.7698 (x + y + 5. z)]^2
```

3D contour plot of the interference pattern. The amplitudes are not optimized, resulting in distorted contours...

```
g = 2;
ack =
  Table[Intensity[xi, yi, zi, 1, 2, 1, 2], {xi, -g, g, .1}, {yi, -g, g, .1}, {zi, -g, g, .1}];
ListContourPlot3D[ack, Contours → {14}, PlotRange → {{0, 20}, {0, 20}, {0, 20}}]
```

```
ListContourPlot3D[ack, Contours → {22}, PlotRange → {{0, 20}, {0, 20}, {0, 20}}]
```

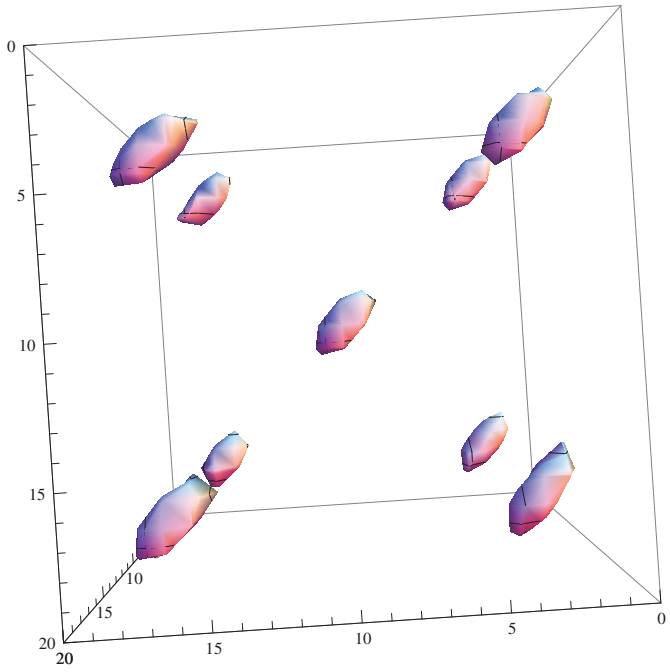

Bibliography

[1] Christopher Foot. *Atomic Physics (Oxford Master Series in Atomic, Optical and Laser Physics)*. Oxford University Press, USA, 1st edition, 2005.

[2] Markus Greiner. *Ultracold quantum gases in three-dimensional optical lattice potentials*. PhD thesis, Ludwig-Maximilians-Universität München, 2003.

[3] R. K Pathria and Paul D Beale. *Statistical mechanics*. Elsevier/Academic Press, Amsterdam, 3rd edition, 2011.

[4] Daniel V Schroeder and John K Pribram. An introduction to thermal physics. *American Journal of Physics*, 67:1284–1285, 1999.

[5] Christopher Pethick and Henrik Smith. *Bose-Einstein Condensation in Dilute Gases*. Cambridge University Press, 2002.

[6] William D Phillips. Laser cooling and trapping of neutral atoms. *Physics, 1996-2000*, 8:199, 2002.

[7] David J Griffiths. *Introduction to Quantum Mechanics*. Pearson Education Limited, 2013.

[8] Harold J Metcalf and Peter Van der Straten. *Laser Cooling and Trapping*. Springer, 1999.

[9] Harold Metcalf and Peter van der Straten. Cooling and trapping of neutral atoms. *Physics Reports*, 244(4):203–286, 1994.

[10] Y-J Lin, AR Perry, RL Compton, IB Spielman, and JV Porto. Rapid production of ^{87}Rb Bose-Einstein condensates in a combined magnetic and optical potential. *Physical Review A*, 79(6):063631, 2009.

[11] Charles Kittel. *Introduction to Solid State Physics*. Wiley, 8$^{\text{th}}$ edition, 2005.

[12] Subhadeep Gupta, Aaron E Leanhardt, Alexander D Cronin, and David E Pritchard. Coherent manipulation of atoms with standing light waves. *Comptes Rendus de l'Académie des Sciences-Series IV-Physics*, 2(3):479–495, 2001.

[13] Roger G Newton. *Scattering theory of waves and particles*. Courier Dover Publications, 1982.

[14] Gretchen Kathleen Campbell. *87 Rubidium Bose-Einstein condensates in optical lattices*. PhD thesis, Massachusetts Institute of Technology, 2006.

[15] Ovidiu Toader, Timothy YM Chan, and Sajeev John. Photonic band gap architectures for holographic lithography. *Physical Review Letters*, 92(4):043905, 2004.

[16] L. Z. Cai, X. L. Yang, and Y. R. Wang. Formation of three-dimensional periodic microstructures by interference of four noncoplanar beams. *Journal of the Optical Society of America A*, 19(11):2238–2244, Nov 2002.

[17] M Campbell. Fabrication of photonic crystals for the visible spectrum by holographic lithography. *Nature*, 404(6773):53–56, 2000.

[18] KI Petsas, AB Coates, and G Grynberg. Crystallography of optical lattices. *Physical Review A*, 50(6):5173, 1994.

[19] Philip Hobbs. *Building Electro-Optical Systems: Making It all Work (Wiley Series in Pure and Applied Optics)*. Wiley, 2$^{\text{nd}}$ edition, 2009.